U.S. Department
of Transportation
**National Highway
Traffic Safety
Administration**

NHTSA

DOT HS 813 671

January 2026

Early Detection of Thermal Runaway With Advanced Diagnostics

This page is intentionally left blank.

DISCLAIMER

This publication is distributed by the U.S. Department of Transportation, National Highway Traffic Safety Administration, in the interest of information exchange. The opinions, findings, and conclusions expressed in this publication are those of the authors and not necessarily those of the Department of Transportation or the National Highway Traffic Safety Administration. The United States Government assumes no liability for its contents or use thereof. If trade or manufacturers' names or products are mentioned, it is because they are considered essential to the object of the publication and should not be construed as an endorsement. The United States Government does not endorse products or manufacturers.

NOTE: This report is published in the interest of advancing motor vehicle safety research. While the report may provide results from research or tests using specifically identified motor vehicle models, it is not intended to make conclusions about the safety performance or safety compliance of those motor vehicles, and no such conclusions should be drawn.

Suggested APA Format Citation:

Torres-Castro, L., Bates, A. M., Johnson, N. B., Quintana, G., Gray, L., Tanim, T., Walker, L., Todd, J. T., & Vennam, G. (2026, January). *Early detection of thermal runaway with advanced diagnostics* (Report No. DOT HS 813 671). National Highway Traffic Safety Administration. https://doi.org/10.21949/w5aa-m571

This page is intentionally left blank.

Technical Report Documentation Page

1. Report No.	2. Government Accession No.	3. Recipient's Catalog No.
DOT HS 813 671		

4. Title and Subtitle	5. Report Date
Early Detection of Thermal Runaway with Advanced Diagnostics	January 2026
	6. Performing Organization Code

7. Author(s)	8. Performing Organization Report No.
Loraine Torres-Castro, Alex M. Bates, Nathan B. Johnson, Genaro Quintana, Lucas Gray, Sandia National Laboratories; Tanvir Tanim*, Lee Walker, Jordan T. Todd, Geetika Vennam	DE-NA0003525

9. Performing Organization Name and Address	10. Work Unit No. (TRAIS)
National Highway Traffic Safety Administration 1200 New Jersey Avenue SE Washington, DC 20590	11. Contract or Grant No.

12. Sponsoring Agency Name and Address	13. Type of Report and Period Covered
National Highway Traffic Safety Administration 1200 New Jersey Avenue SE Washington, DC 20590	Final Report
	14. Sponsoring Agency Code

15. Supplementary Notes

This work was funded by the United States Department of Transportation, National Highway Traffic Safety Administration. This report was written by SNL, managed, and operated by National Technology & Engineering Solutions of Sandia, LLC, a wholly owned subsidiary of Honeywell International Inc., for the U.S. Department of Energy's National Nuclear Security Administration under contract DE-NA0003525, and INL, operated by Battelle Energy Alliance, LLC, with the U.S. Department of Energy under Contract No. DE-AC07-05ID14517.

Digital Object Identifier: https://doi.org/10.21949/w5aa-m571

16. Abstract

In support of NHTSA's vehicle safety mission, this report investigates the state-of-the-art in early detection of thermal runaway in Li-ion battery packs contained in electric vehicles (EVs). This work uses an open-architecture test-demonstration platform to aid in the characterization of four battery safety sensors that can be used for EVs.

This report focuses on employing rapid electrochemical impedance spectroscopy (EIS), volatile organic compound (VOC) sensing, and H2 gas sensing technology to monitor cells and battery packs for signs of failure. Experimental results with individual cells and packs subjected to thermal or electrical abuse reveal that rapid EIS and VOC sensors provide earlier warning of thermal runaway compared to H2 sensors. Furthermore, it was demonstrated that the implementation of rapid EIS and VOC sensor monitoring enables the detection and prevention of thermal runaway. The study also delves into how these sensors respond based on cell chemistry (lithium nickel manganese oxide, lithium iron phosphate), capacity, and system engineering (heat transfer). Additionally, the report discusses the challenges with integrating sensor systems in large EV battery packs, including issues with signal-to-noise for impedance sensors or placement of VOC sensors in larger packs.

17. Key Words	18. Distribution Statement
Li-ion, battery pack, thermal runaway, electric vehicle, gas sensing	Document is available to the public from the DOT, BTS, National Transportation Library, Repository & Open Science Access Portal, https://rosap.ntl.bts.gov.

19. Security Classif. (of this report)	20. Security Classif. (of this page)	21. No. of Pages	22. Price
Unclassified	Unclassified	67	

Form DOT F 1700.7 (8-72) Reproduction of completed page authorized

This page is intentionally left blank.

Table of Contents

Introduction **1**

Experimental Methods for the Evaluation of Battery Diagnostics **3**

Abuse Testing Methods 3
Gas Sensor Parameter Optimization 5

Results and Discussion **9**

Evaluating VOC Sensor During Major Abuse Scenarios With Energy Density, Manufacturer, and Chemistry 9
Energy Density & Cell Engineering 9
Cell Chemistry 11
Effect of Fixturing in Thermal Runaway Response 12
Overtemperature Failure Initiation 13

Overtemperature Failure in Single Cells 13
Overtemperature Failure in a 1s4p Pack Configuration 19

Overcharge Failure Initiation 23

Overcharge Failure in Single Cells 24
1s4p Overcharge Failure in a 1s4p Pack Configuration 27
Overcharge Failure in a 2s4p Pack Configuration 30

Intervention at Identified Failure Markers 32

Overtemperature Failure Intervention 32
Overcharge Failure Intervention 34

Conclusions **37**

References **39**

Appendix A: Battery Advanced Diagnostics Evaluation (Badge) Platform **A-1**

Battery Advanced Diagnostics Evaluation (Badge) Platform A-2

BADGE Concept A-2
BADGE Platform Development A-3

List of Figures

Figure 1 . Schematic of the test setup for overtemperature testing.....5
Figure 2. (a) Schematic of VOC sensors placement within the testing bay, the distance of each sensor from the tested cell, and triggering time. (b) The physical location of the sensors within the bay.....6
Figure 3. Sensor trigger timing compared to cell thermal runaway, 10 Ah NMC cell during overtemperature test with a heating rate of 5 °C/min; (a) voltage and temperature profile, and (b) sensor trigger timing based on sensor locations. 7
Figure 4. (a) Runaway enthalpy as a function of energy in Wh. (b) Peak runaway temperatures as a function of the cell specific energy.....10
Figure 5. (a) voltage and temperature response during OT tests for gr/NMC pouch cell from Manufacturer A and Manufacturer B; (b) heating rate and sensor triggering time for Manufacturer A; and (c) heating rate and sensor triggering time for Manufacturer B.....10
Figure 6. (a) voltage and temperature response during OT tests for NMC/gr, and LFP/gr pouch cells, (b) heating rate and Li-ion Tamer sensor triggering time for LFP/gr; and (c) heating rate and sensor triggering time for NMC/gr.....11
Figure 7. Evaluation of electrical failure behavior and Li-ion Tamer sensor triggering time for: (a) 10 Ah LFP/gr cells; and (b)10Ah NMC/gr cells. 12
Figure 8. Evaluation of electrical failure behavior and VOC sensor triggering time for NMC cells constrained with brass blocks and phenolic plates: (a) voltage and temperature response during OC failure; (b) heating rate; and (c) sensor triggering time. 13
Figure 9. (a) Temperature and voltage response of a single 11.6 Ah NMC cell during an overtemperature test, (b) heating rate and time resolved FTIR measurements and (c), before and (d) after failure test images. 14
Figure 10. Voltage differential during the OT test in Figure 9 show only perturbations due to rapid EIS measurements with no indications of damage to the cell. 14
Figure 11. FTIR absorbance spectra at 24.28 min of the single cell subjected to overtemperature testing.....15
Figure 12. Commercial gas sensors response during overtemperature test of an 11.6 Ah pouch cell.....16
Figure 13. Time-resolved mass spectrometry during overtemperature test of a 11.6 Ah pouch cell.....17
Figure 14. (a) Qualitative graphical representation of rapid EIS failure marker (solid blue star) during abusive conditions, and (b) rapid EIS response during OT test of a 11.6 Ah single pouch cell. 18
Figure 15. Full frequency spectrum Nyquist plots collected during the single cell overtemperature abuse test at the start of the test, the 0.1 Hz impedance magnitude minimum, the failure marker as defined in the main text, and onset of thermal runaway.....19
Figure 16. Temperature and voltage response of an overtemperature test of the edge cell within a 1s4p battery pack (left). The thermocouple map (middle) and thermal runaway video still (right) are also illustrated. 20

Figure 17. (a) Gas sensor and (b) rapid impedance spectroscopy measurements during an over temperature test of the edge cell within a 1s4p battery pack. 21
Figure 18. Full frequency spectrum Nyquist plots collected during the 1s4p overtemperature abuse test at the start of the test, the 0.1 Hz impedance magnitude minimum, the failure marker as defined in the main text, and onset of thermal runaway. 22
Figure 19. (a) Temperature and voltage response of a single 11.6 Ah NMC cell during overcharge conditions, (b) heating rate and time-resolved FTIR measurements, and (c), (d) pre and post failure test images. 24
Figure 20. Gas sensor response during overcharge tests of a 11.6 Ah pouch cell. 25
Figure 21. Time-resolved mass spectrometry collected during overcharge test of a 11.6 Ah pouch cell. 25
Figure 22. Rapid EIS response during overcharge test of an 11.6 Ah pouch cell. 26
Figure 23. Full frequency spectrum Nyquist plots collected during the single cell overcharge abuse test at the start of the test, the 0.1 Hz impedance magnitude minimum, the failure marker as defined in the main text, and thermal runaway. 27
Figure 24. Temperature and voltage response during overcharge of a 1s4p battery pack (left). A schematic representation of the unit under investigation (middle) and test setup photograph (right) are also included. 27
Figure 25. (a) Gas sensor and (b) rapid impedance spectroscopy measurements during overcharge failure of a 1s4p battery pack. 28
Figure 26. Full frequency spectrum Nyquist plots collected during the 1s4p cell overcharge abuse test at the start of the test, the 0.1 Hz impedance magnitude minimum, the failure marker as defined in the main text, and thermal runaway. 29
Figure 27. (a) Temperature and voltage response during overcharge of a 2s4p battery pack, and (b) zoomed-in section of panel (a). (c) A schematic representation of the unit under investigation and (d) during/post-tests photographs. 31
Figure 28. (a) Gas sensor and (b) rapid impedance spectroscopy measurements during overcharge failure of a 2s4p battery pack. 31
Figure 29. Full frequency spectrum Nyquist plots collected during the 2s4p cell overcharge abuse test at the start of the test, the 0.1 Hz impedance magnitude minimum, the failure marker as defined in the main text, and thermal runaway. 32
Figure 30. Voltage and temperature response of a 1s4p battery pack during overtemperature test (left). The thermocouple array (middle) and tests setup images (right) are also presented. In this test, the heating element was deactivated when a failure marker was identified. 33
Figure 31. In-operando diagnostics measurements during overtemperature failure of a 1s4p battery pack:(a) COTs gas sensors, and (b) rapid EIS. 33
Figure 32. Intervention based on diagnostics response during overcharge of a 1s4p battery pack. (a) Voltage and temperature profile, and (b) COTs gas sensors measurements. 34
Figure 33. The time-resolved magnitude of impedance at 0.1 Hz for the 1s4p intervention test. 35
Figure 34. Conceptual layout of the BADGE platform. A-2
Figure 35. BMS functionality and communication capability. A-3

Figure 36. Hardware components procured for the BADGE platform. A-4
Figure 37. BADGE platform developed at INL for comprehensive battery pack diagnostics. .. A-5
Figure 38. Graphical user interphase of the BADGE platform. A-6
Figure 39. LabVIEW block diagram used to control the SMU. A-7

List of Tables

Table 1. Specifications for pouch cells discussed in this document. 3
Table 2. $\Delta t_{warning\ time}$ for single cell and pack level testing during over temperature conditions (single data points). 23
Table 3. $\Delta t_{warning\ time}$ for 11.6Ah NMC pouch cells during OC conditions: cell and pack level testing (single data points). 29

List of Acronyms/Definitions

LIB	lithium-ion battery, also called a Li-ion battery
BMS	battery management system
EV	electric vehicle
EIS	electrochemical impedance spectroscopy
VOC	volatile organic compound
SOC	state-of-charge
INL	Idaho National Laboratory
IMB	impedance measurement box
OT	overtemperature
OC	overcharge
DAQ	data acquisition
TC	thermocouple
PXI	peripheral component interconnect eXtensions for instrumentation
CAN	controller area network
LIN	local interconnect network
SMU	source measure unit
NMC	lithium nickel manganese cobalt oxide
FTIR	Fourier-transform infrared spectroscopy
MS	mass spectrometry
PID	proportional-integral-derivative
LFP	lithium iron phosphate
SEI	**s**olid electrolyte interphase

Introduction

Li-ion battery failure can emerge suddenly under diverse conditions including charging, active operation, or even during periods of inactivity (Hendricks et al., 2015; Feng et al., Larsson & Mellander, 2014; Wang et al., 2012). Existing battery management systems (BMS) are not well equipped to detect thermal runaway failure until that failure is inevitable (Habib et al., 2023; Challoob et al., 2023; Sanitha et al., 2022; Mishra et al., 20121, Balasingam et al., 2020). During circumstances in which a cell is on the track to thermal runaway, the limited BMS capability does not allow for intervention and, in the worst cases, provides unacceptable warning times to electric vehicle occupants (Dong et al., 2021; Jin et al., 2020; Ren et al., 2017). Thus, diagnostics that can offer early warning to LIB failure must be further evaluated, for the possible implementation in EV battery packs.

Abuse of cells and batteries (e.g., from fast charge, manufacturing defects, etc.) can have a wide range of consequences depending on the type and severity of the damage caused, and the properties of the battery itself (Baakes et al., 2022; Duan et al., 2022; Li et al., 2023; Q. Wang g et al., 2019; Y. Wang g et al, 2018, Xia et al., 2023). Cell stability is dependent on both a cell's health and its safety. This includes factors such as potential failure modes and structural integrity throughout the life cycle of the cell as well as the available capacity relative to its initial state. The most common technique for establishing cell stability, using modern BMS technology, involves monitoring temperature and voltage as a function of state-of-charge during operation (Wei et al., 2019; Xia et al., 2016). For abusive conditions, however, this measurement can be a poor indicator as it does not always give enough warning time prior to a catastrophic thermal runaway event (Liao et al., 2019)]. Modern systems often lack the sensitivity and resolution to measure cell degradation markers until failure is imminent. For LIBs, it is particularly difficult to determine cell stability with the purpose of predicting thermal runaway because the voltage profile typically retains a uniform profile, until moments before cell failure (Ishikawa, et al., 2011). Once a voltage or temperature change is significant enough to be identified, catastrophic thermal runaway is likely unavoidable, often with little to no effective means of suppression or mitigation (Abraham et al., 2006; Doughty et al., 2022; Lamb & Orendorff, 2014; Xu et al., 2012; Spotnitz et al., 2007; Jhu et al., 202011). Early detection of degradation markers and point of failure identification is essential to the prevention of catastrophic failure.

Electrochemical impedance spectroscopy is one potential tool to determine the stability of an electrochemical cell or battery pack (Lyu et al., 2022; Srinivasan et al., 2011, 2018) A major limitation of this technique is the inability to perform measurements of dynamic systems where cell conditions (e.g., temperature or voltage) are changing (Messing et al., 2021)]. EIS requires a pseudo-linear steady-state system as changes in voltage or temperature can introduce harmonics resulting in noisy and unreliable data. This has historically limited the use of impedance to time-consuming full spectra measurements of batteries at rest or measurements of an active battery at a single high frequency (e.g., 1000 Hz) (Carkhuff et al., 2016; Giegerich et al., 2016; Waag et al., 2014). Keeping a battery pack at rest long enough to perform full spectra EIS measurements is not always reasonable, and single frequency measurements generally yield limited information for advanced diagnostics in dynamic systems.

Idaho National Laboratories and Montana Technological University led the development of a specialized impedance measurement box capable of capturing impedance spectra at several discrete frequencies in ten-to-fifteen second intervals (Christophersen et al., 2012). The IMB prototype was commercialized by Dynexus as the iRIS P1-02, which was used in this work. The

fast collection of EIS data is essential for adequately establishing accurate failure markers and using EIS as an onboard diagnostic. However, the response of IMB may be limited when transitioning from single cells to multi-cell packs (Beelen et al., 2020; Raijmakers et al., 202016). As a result, EIS analysis will likely need to be supplemented with non-electrochemical diagnostics (Essl et al., 20, 2021)]. Non-electrochemical diagnostics can aid in more accurately determining the stability of battery systems and monitor for warning signs of cell failure. Gas sensing can provide early warning detection that is especially useful when you have hundreds to thousands of cells, such as within an EV pack (Liao et al., 2019; Cai et al., 2019). Detectable gases during thermal runaway are typically volatile organic compounds resulting from electrolyte solvents (e.g., ethylene carbonate, ethyl methyl carbonate, diethyl carbonate, dimethyl carbonate), carbon dioxide (CO_2), and hydrogen (H_2) (Gachot et al., 20, 2011; Golubkov et al., 202014; Lammer et al., 2017).

In this work, commercial gas sensors and rapid EIS are evaluated to identify failure warning times as cells undergo thermal and electrical abuse. Signals obtained through rapid EIS and gas-sensing are correlated with live sampling using Fourier transform infrared spectrometry and mass spectrometry. FTIR and MS gas analysis provides a deeper understanding of abused cell failures and forms the technical basis for diagnostics that could ultimately be used for early detection. During these tests, markers are identified in EIS data and gas-based sensor data that correspond to the onset of unstable conditions. The combination of gas sensing and rapid EIS could provide early warning of impending catastrophic failure to potentially mitigate the consequences of manufacturing irregularities (Case, 2022), accidents (Rask et al., 202020; Zhang et al., 2022), and natural events (e.g., salt-water flood damage) (Gutman et al., 2022).

Experimental Methods for the Evaluation of Battery Diagnostics

Abuse Testing Methods

To evaluate the diagnostic tools and identify failure markers, cells were taken to the point of thermal runaway via two pathways, overtemperature and overcharge. Nail penetration initiation method was briefly explored, but there were no signs of imminent failure until the cell was on full thermal runaway. Additional testing was done to explore the impact of cell design parameters on abuse, including variations in cell chemistry, capacity, and manufacturer. There were 11.6-Ah lithium nickel manganese cobalt oxide pouch cells (Kokam, Part# SLPB065070180) used for testing either single cells, 1s4p, or 2s4p packs where "s" indicated the number of cells in series and "p" indicates the number of cells in parallel (cell specifications in Table 1). Single cells and packs were assembled using fixturing plates, phenolic or brass, and bolts on each corner. This is to hold the pack assembly together but not impact the integrity of the cells or influence the outcome by applying significant pressure. K-type thermocouples (Omega, 36 gauge) were placed on each cell, and between fixturing plates and cell. For all tests, the cells were brought up to 100 percent SOC prior to test initiation. Charging to 100 percent SOC was accomplished by using a constant current with a C-rate of C/2 until the cell reached 4.2 V, then applying a taper charge at a constant voltage of 4.2 V until the current reduced to C/20.

Table 1. Specifications for pouch cells discussed in this document.

Kokam NMC Pouch Cell (Manufacturer A)								
Capacity (Ah)	**Dimensions (mm)**			**AC-IR (mOhm)**	**Weight (kg)**	**Discharge Rate**		**Energy Density (Wh/kg)**
	W	**L**	**T**			**C-rate (C)**		
						continuous	**Pulse**	
11.6	84	185	6.6	2.8	0.17	2	4	246
Battery Space NMC Pouch Cell (Manufacturer B)								
Capacity (Ah)	**Dimensions (mm)**			**AC-IR (mOhm)**	**Weight (kg)**	**Discharge Rate**		**Energy Density (Wh/kg)**
	W	**L**	**T**			**C-rate (C)**		
						continuous	**Pulse**	
10	91	141.2	9.2	8	0.226	0.2	2	175
Battery Space LFP Pouch Cell								
Capacity (Ah)	**Dimensions (mm)**			**AC-IR (mOhm)**	**Weight (kg)**	**Discharge Rate**		**Energy Density (Wh/kg)**
	W	**L**	**T**			**C-rate (C)**		
						continuous	**Pulse**	
10	92.5	163	8.9	10	0.250	5	10	152

During all tests, the cells were connected to an IMB rapid EIS system (Dynexus Technology, iRIS P1-02). All EIS measurements were taken for the range of 0.1Hz to 1638 Hz (the upper limit of the rapid EIS equipment is 2 khz). EIS measurements during OC were taken at an interval rate of 5 percent SOC, while during OT testing measurements were taken every 60 seconds for single cells, and every 20 seconds for 1s4p and 2s4p assemblies. The change in sampling rate to 20s for packs was the result of a need for increased sampling resolution on subsequent tests after testing the single cells at a sampling rate of 60s. For the purposes of data representation, the time-resolved magnitude of impedance at 0.1 Hz is shown in this paper, but full spectrum EIS data for each test is also shown. The EIS failure marker was defined as the first point of increasing impedance magnitude after a minimum. In other words, the failure marker is when the first derivative of the impedance with respect to time changes sign from negative to positive.

Gas sensors were mounted 22.9 cm from the cells. The details on how this specific distance was determined are discussed further in the next section. Three gas sensors with different proprietary gas detection methods were used. These sensors are a VOC gas detector (Li-ion Tamer, Part# 241022), a combined VOC, CO_2, and H_2 sensor (Metis Engineering, Part# CANBSSGEN1), and an H_2 sensor (Amphenol, Part# AX221058). The VOC detector, consistent with EPA 40 CFR 51.100,[1] was connected to a proprietary monitoring device, which outputs a digital signal that was received by a data acquisition system. Voltage sensing for all tests was also routed to the same DAQ. The combined gas sensor collects data in ppb for VOC, and in ppm for CO_2 and H_2, and transmits that data via controller area network bus where it was retrieved using a LabVIEW DAQ card and LabVIEW based software. The H_2 sensor's gas detection method is via thermal conductivity. The H_2 sensor outputs an analog signal that was also collected by a LabVIEW DAQ card and using LabVIEW based software. The function of each gas sensor was validated prior to each test using acetone (a VOC) for the VOC and combined gas sensors, and helium (similar thermal conductivity to H_2) for the H_2 sensor. In addition, for single cell testing, two gas composition detectors were continuously operated including FTIR (Thermo Fisher Scientific, Nicolet iS50) and MS (Thermo Fisher Scientific, Prima δB). The FTIR uses a gold KBr beam splitter with a process flow rate of 500 cm^3 min^{-1}. The MS uses a 2.4 – 2.9 A thoria coated iridium filament with a 0.3 mm inner diameter capillary tube. The failure marker for gas detection was defined as the activation of each respective sensor represented as a drop in voltage for the VOC sensor or an increase in the analog voltage signal for the combined gas and H_2 sensors.

Thermal runaway initiation via OT was carried out by fixturing either a single cell or a 1s4p pack between two brass plates (each 15.2 cm x 10.2 cm, 0.1 cm thick). Two cartridge heaters (Tutco Part# CH11456, 300 W, 15.2 cm in length, 0.6 cm diameter) were placed on one brass plate (see Figure 1) to examine the effect of targeting thermal runaway in one side of the cell or in one cell within a pack (the cell adjacent to the heated brass plate). During all OT tests, the temperature ramp rate was controlled to 5°C/min using a proportional-integral-derivative controller. The PID loop is fed a temperature from a K-type TC that resides between the brass plate and battery cell, positioned at the center of the cell to keep the heating rate of the cell constant. Note that this TC reading is not saved and is therefore not reported in this work. The same TCs were used

[1] A.k.a. the Clean Air Act (42 U.S.C. 7401 et seq., as amended by Pub. L. 91-604, 84 Stat. 1676 Pub. L. 95-95, 91 Stat., 685 and Pub. L. 95-190, 91 Stat., 1399).

throughout all testing, including the OC initiated thermal runaway tests. The TCs were first wrapped in a single layer of polyimide electrically insulating tape (Kapton). Then the TC was placed in the specified location using an additional layer of Kapton tape. This prevents TCs from slipping out of place during test assembly and operation.

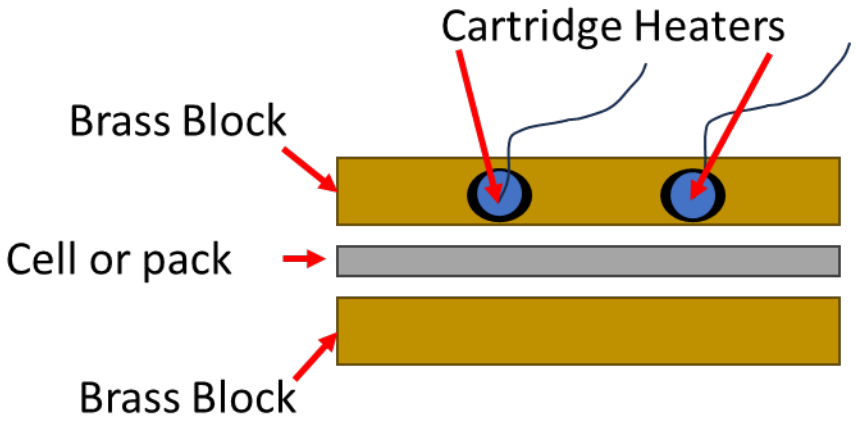

Figure 1. Schematic of the test setup for overtemperature testing

Thermal runaway initiation via OC was carried out by fixturing a single cell, 1s4p pack or 2s4p pack between two phenolic resin plates (15.2 cm x 15.2 cm, 1.3 cm thick). Phenolic plates are used for OC because they are thermally insulating. This better replicates conditions that are relevant to a scenario where cells are placed in packs and/or casing that does not have the conductive heat transfer that would occur with metal fixturing plates (e.g., brass plates). The unit under test was then connected to a power supply (Hewlitt Packard PN# 6032A, 0 to 50 A, 1000 W) to supply the current necessary for the OC condition. In this work, all cells were charged to 100 percent SOC prior to the start of the OC test. The OC condition was held at 1C until the cell failure was observed; the capacity was 11.6 Ah for single cells and 46.4 Ah for 1s4p pack-level testing.

Gas Sensor Parameter Optimization

Gas sensor parameter optimization was carried out using 10 Ah NMC pouch cells (Battery Space, Part# 8790140; cell specifications in Table 1) where the time delay associated with sensor location was quantified. The diagnostic device used for this purpose was the VOC sensor, which is meant to primarily identify vaporized electrolyte solvent after cell rupture. The sensors were placed in the array shown in Figure 2(a). Sensor 1 was situated within a few centimeters of the cell. Sensors 2, 3, and 5 were extended in a straight line from the edge of the testing box to the bay door. Sensor 4 was located near the makeup air intake, and Sensor 6 was located beneath the bay door, where there is a gap between the door and the floor. A significant amount of airflow may be present within the testing bay (43 air exchanges per hour), which may impact the ability of a sensor to detect cell off-gassing. In Figure 2(b), the physical locations within the test bay of Sensors 1 and 2 (left), Sensors 2, 3, and 5 (middle), and Sensor 4 (right), are shown.

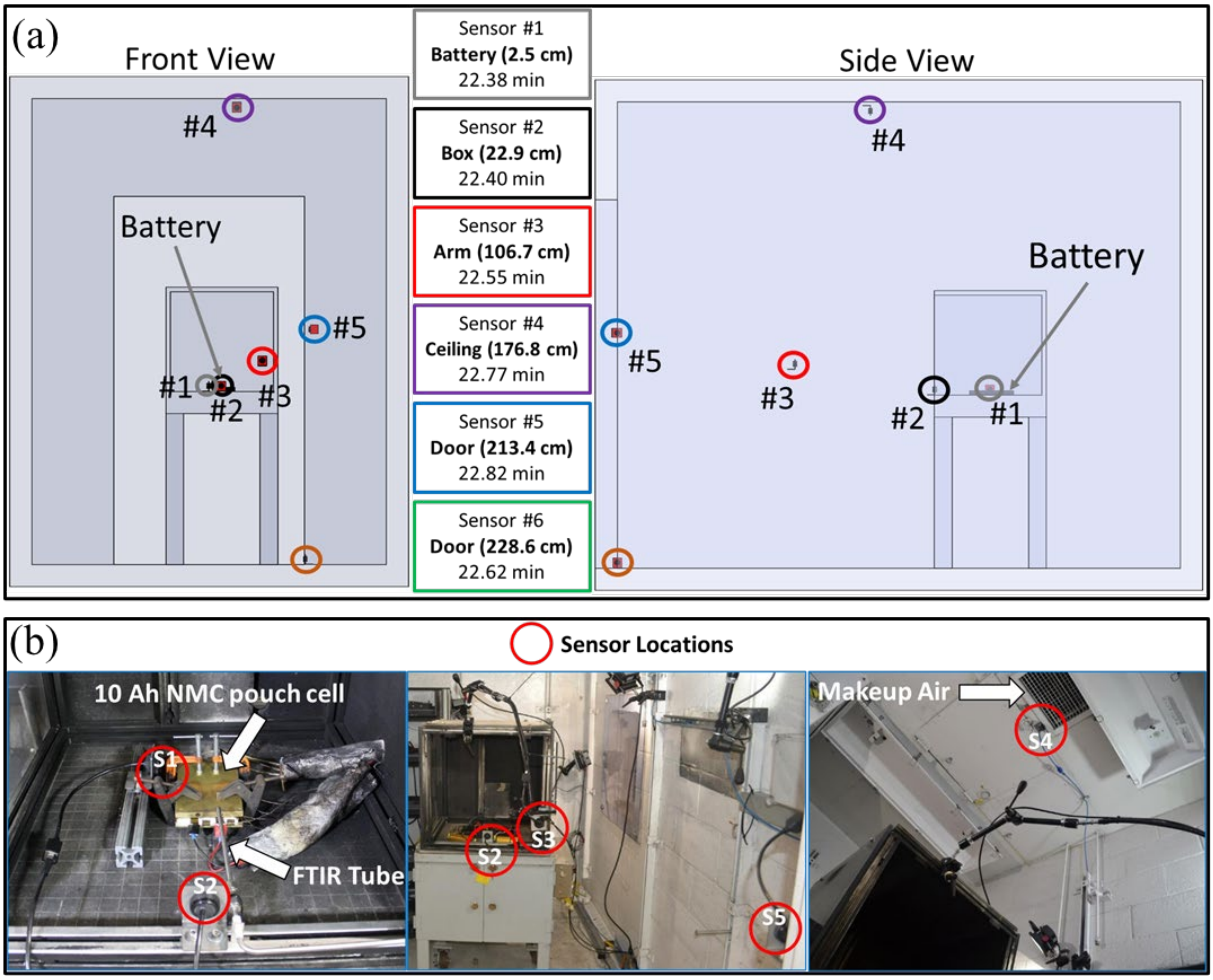

Figure 2. (a) Schematic of VOC sensors placement within the testing bay, the distance of each sensor from the tested cell, and triggering time. (b) The physical location of the sensors within the bay

An OT test was conducted with a 10 Ah NMC pouch cell and the sensor configuration shown in Figure 2. The cell temperature and heating rate are presented in Figure 3(a). The use of heating rate is critical as the values measured by a TC are dependent on events within the cell that can affect heat transfer properties and sensor trigger time. As shown in Figure 3(b), the sequence of triggers for sensors 1, 2, and 3 were as expected, with sensor 1 triggering first, followed by sensor 2. Sensor 3 triggered 10 seconds later. Sensors 4 through 6 were sensitive to the air flow dynamics of the room, with the sensor closest to the makeup air vent (sensor 4) being the last to trigger. The makeup air vent continuously pushes air into the test bay. Sensor 6 triggered before 4 and 5 due to air flow through the space between the bottom of the door and the floor.

Although all sensors triggered within 36 seconds of the first sensor triggering, across two repeat tests, as shown in Figure 3(b), sensor location does have a measurable effect on response, with sensors closest to the test cell triggering first. Therefore, all sensors used in subsequent tests were placed 22.6 cm from the cell to minimize transport phenomena issues and to prevent damage to the sensor during thermal runaway.

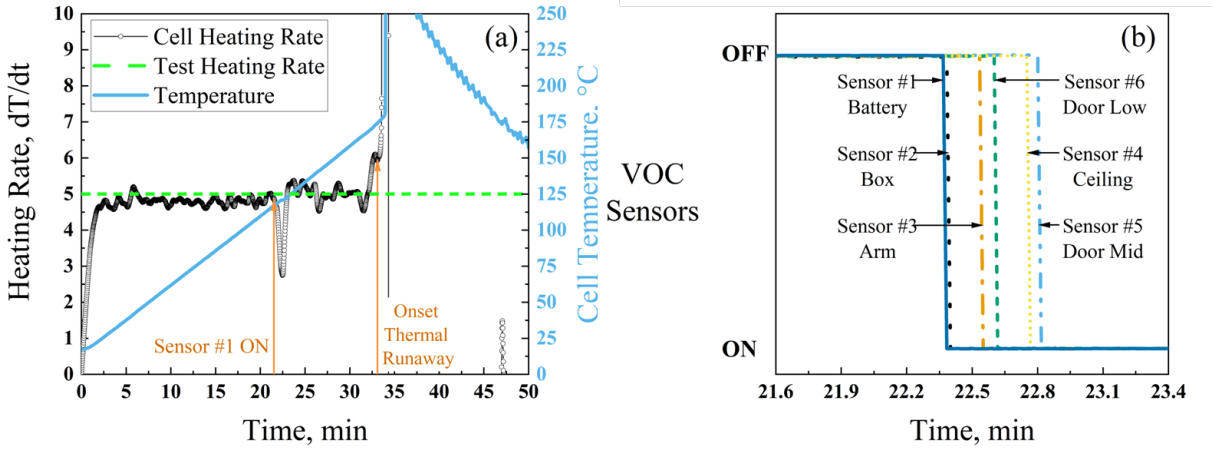

Figure 3. Sensor trigger timing compared to cell thermal runaway, 10 Ah NMC cell during overtemperature test with a heating rate of 5 °C/min; (a) voltage and temperature profile, and (b) sensor trigger timing based on sensor locations

This page is intentionally left blank.

Results and Discussion

To characterize the capability of rapid EIS and commercially available gas sensors as diagnostic techniques for early warning detection, the response of each technique during thermal (OT) and electrical (OC) failures was evaluated. Key metrics evaluated were onset temperature of cell venting for thermal failures, and onset SOC of thermal runaway for electrical failures. The onset values for thermal failures were determined when the derivative of temperature with time (heating rate) exceeded > 5 °C/min. Metrics that applied to both failure modes were onset temperature of thermal runaway, onset time of thermal runaway (TRtime), time of sensor activation (Sactivation time), and warning time (Δtwarning time). The warning time was calculated using Equation 1.

$$\Delta t_{warning\ time} = TR_{time} - S_{activation\ time} \quad (1)$$

Evaluating VOC Sensor During Major Abuse Scenarios With Energy Density, Manufacturer, and Chemistry

We demonstrated the feasibility of the VOC sensor to provide early detection of single pouch cell venting on the occurrence of a fault that leads to thermal runaway. To characterize the sensitivity of the VOC gas sensors, we evaluated the response of the VOC sensor during thermal and electrical failures of single cells with different: (1) energy density + manufacturer; (2) chemistry; and (3) fixturing (only for electrical failure), where *fixturing* refers to the materials that hold the cell in place (single cell) or together (pack).

Energy Density & Cell Engineering

Cell energy density (Wh/kg) and cell engineering have been demonstrated to significantly affect the safety response of Li-ion batteries during abusive scenarios. Sandia has evaluated the safety characteristics of thousands of cells with different chemistries, energy densities, and form factors. These variations influence the energetics (total heat and pressure release, gas generation), heat dissipation, and maximum temperatures during thermal runaway. In Figure 4, published work from our team validates that total heat release is strongly correlated with the stored energy available (Figure 4(a)), but peak temperatures during thermal runaway are more closely related to energy density (Figure 4(b)) (Lamb et al., 2021). Hence, it is imperative that we comprehend the impact of these variables on the suitability of gas sensors for on-board diagnostics.

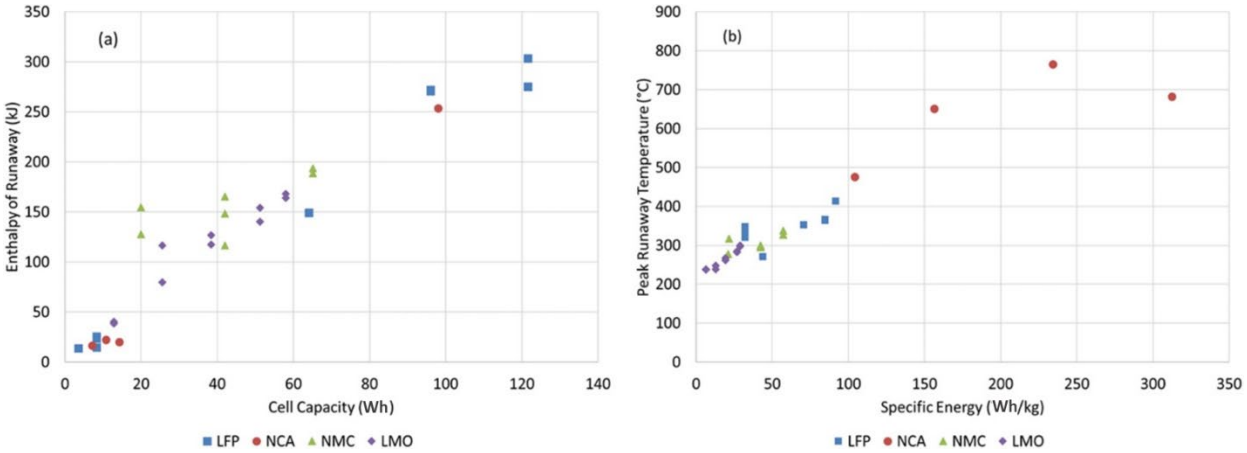

Figure 4. (a) Runaway enthalpy as a function of energy in Wh. (b) Peak runaway temperatures as a function of the cell specific energy

To evaluate the impact of energy density and manufacturer on the response of the VOC gas sensor (Li-ion tamer), we conducted OT tests on NMC/gr single cells from two distinct manufacturers: (1) manufacturer A (Kokam, Part# SLPB065070180) with 246 Wh/kg and (2) manufacturer B (Battery Space, Part# 8790160) with 185 Wh/kg. The cells were instrumented with heaters on both sides of the cell, and the temperature was increased at 5 °C/min. As shown in Figure 5(a), cell venting occurred at similar temperatures for both cells, with manufacturer A venting at 125 °C and manufacturer B at 117 °C. The onset to thermal runaway was 142 °C for manufacturer A and 174 °C for manufacturer B. Sensor warning time is shown in Figure 5(b) and Figure 5(c), comparing the sensor trigger time to the cell heating rate (°C/min). The sensors for both cells triggered during cell venting with a $\Delta t_{warning\ time}$ of 3 min and 11 min, respectively, for manufacturers A and B. Attributing the discrepancy in $\Delta t_{warning\ time}$ is beyond the work scope but may be associated with variances in cell design such as physical dimensions, electrolyte additives, and electrode stoichiometry. Therefore, energy density and cell engineering are key characteristics to consider when evaluating the feasibility of gas sensors as a technique for early detection of thermal runaway.

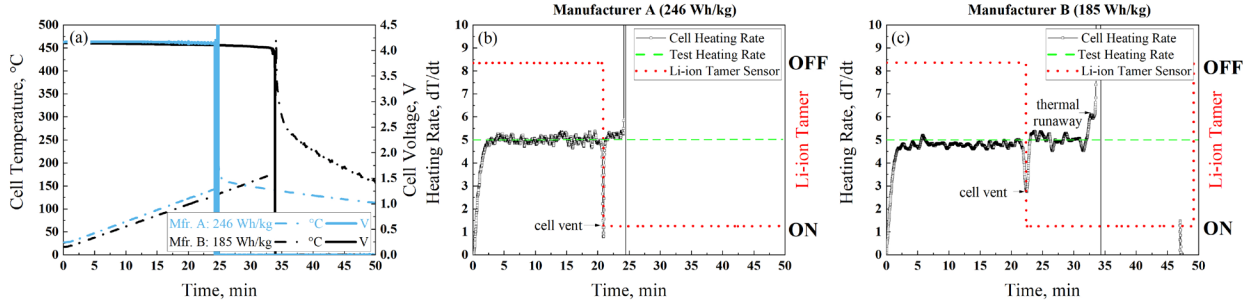

Figure 5. (a) voltage and temperature response during OT tests for gr/NMC pouch cell from Manufacturer A and Manufacturer B; (b) heating rate and sensor triggering time for Manufacturer A; and (c) heating rate and sensor triggering time for Manufacturer B

Cell Chemistry

The tolerance of cell chemistry to a variety of abuse conditions, including overcharging, over-discharging, overheating, and physical damage, is contingent upon their inherent chemical compositions, thermal stability, and engineering. In lithium iron phosphate cells, enhanced thermal stability is largely a function of the resilient covalent bond present within the iron phosphate (FePO4) structure. These bonds make it more difficult for the material to break down. The inherent stability of LFP chemistry results in a higher threshold for thermal runaway. On the contrary, the presence of nickel and cobalt in NMC results in a decrease in thermal stability, potentially leading to more exothermic reactions during thermal runaway as well as a lower onset temperature. Moreover, the stoichiometry of NMC has the potential to significantly influence its thermal runaway characteristics. Higher nickel content often leads to higher energy density but reduces thermal stability. Higher nickel content NMC is also capable of charging to lower lithiation states which can result in greater oxygen release. Cobalt, on the other hand, improves thermal stability but could exacerbate thermal runaway once it has initiated due to its chemical instability up degradation. Considering these variables, we assessed the gas sensor response under thermal and electrical abuse conditions for 10 Ah NMC/gr and 10 Ah LFP/gr cells with similar cell engineering design and assembly (cells specifications in Table 1). The cells were charged to 100 percent SOC using a constant current with a C-rate of C/2 until the cell reached 4.2 V for NMC and 3.8 V for LFP, then applying a taper charge at that voltage until the current reduced to C/20.

Figure 6 shows the (a) temperature and voltage profiles, and (b) heating rate and gas sensor signal for LFP and (c) NMC. The LFP cell was subjected to overheating up to 250 °C without any thermal runaway; however, the complete voltage loss occurred at a temperature of 176 °C, as seen in Figure 6(a). The cell experienced venting at 129 °C, 24 minutes after the test was initiated (Figure 6[b]). A modified version of Equation 1 was used to calculate $\Delta t_{warning\ time}$ since the LFP cell did not experience thermal runaway. The time at which the cell lost complete voltage was used as the value for TR_{time}. Hence, the $\Delta t_{warning\ time}$ for LFP during OT failure was calculated to be 11 minutes, which was the same as for the NMC cells; however, thermal runaway did not occur in the LFP cell.

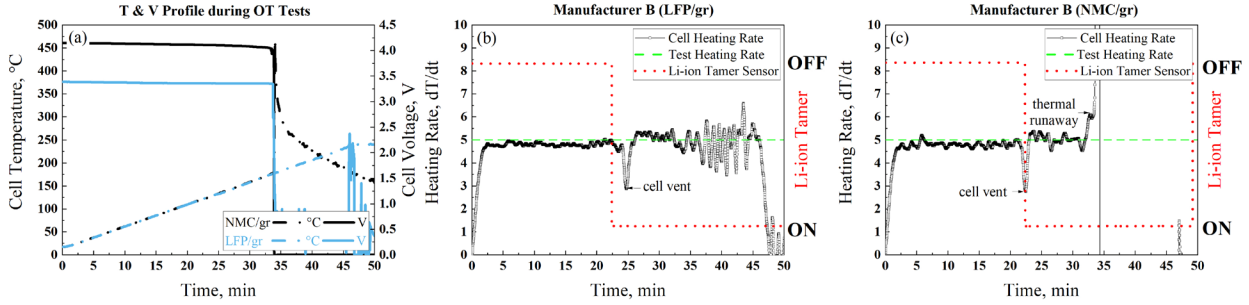

Figure 6. (a) voltage and temperature response during OT tests for NMC/gr, and LFP/gr pouch cells, (b) heating rate and Li-ion Tamer sensor triggering time for LFP/gr; and (c) heating rate and sensor triggering time for NMC/gr

The electrical abuse response was also compared for the NMC and LFP cells, as seen in Figure 7. To maintain cell integrity during OC conditions, the cells were constrained using phenolic plates, as gas generation and cell swelling are expected outcomes of the test. LFP cells have a lower voltage window compared to NMC and overcharging them can more quickly push them

out of their stable operating voltage window (Bates et al., 2021). This could lead to electrolyte decomposition, gas generation, and an earlier onset of thermal runaway relative to NMC. Nonetheless, the chemical and structural instability of NMC coupled with its higher energy density results in elevated temperatures and accelerated heating rates during failure. This behavior was observed during the controlled OC testing, where the onset SOC to thermal runaway was 142 percent for LFP and 173 percent for NMC. Furthermore, as shown in Figure 7(a), the maximum temperatures were significantly different, with NMC reaching 546 °C and LFP < 146 °C. Figure 7(b) and (c) shows the heating rate and gas sensor signal as a function of time. The sensor for LFP triggered earlier at 124 percent SOC, while the NMC sensor triggered at 160 percent SOC. The warning time was 11 minutes for LFP, while the NMC warning time was only 8 minutes. In the case of OC, both the LFP and NMC cells experienced thermal runaway.

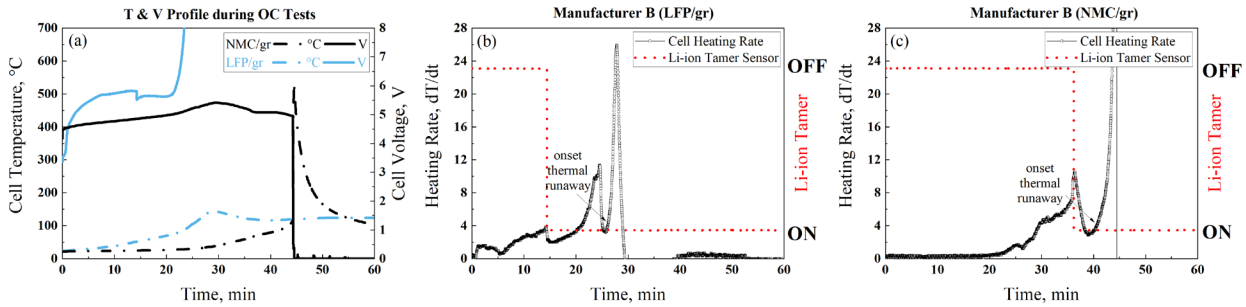

Figure 7. Evaluation of electrical failure behavior and Li-ion Tamer sensor triggering time for: (a) 10 Ah LFP/gr cells; and (b)10Ah NMC/gr cells

The sensor response variation, as a function of cell chemistry, was determined to be minimal for thermally abusive conditions and significant for electrically abusive conditions. This was due to the minimal tolerance of LFP to charge above 3.8 V (maximum voltage), which is attributed to the delithiation state of the cathode at 100 percent SOC.

Effect of Fixturing in Thermal Runaway Response

To characterize OC failure with packaging components with different heat transfer, the OC test was done with brass blocks and phenolic plates as constraints, as shown in Figure 8(a). The 10 Ah NMC/gr cells with brass blocks had an onset SOC to thermal runaway of 222 percent (125 °C), whereas the same cells with phenolic plates had an onset of 171 percent (118 °C). Brass blocks have higher thermal conductivity than phenolic plates resulting in higher heat dissipation. Although thermal runaway occurred at different states of charge and different temperatures (brass blocks – 38 °C, phenolic plates – 64 °C) for the different plates, the gas sensors triggered at the same time/%SOC (e.g., 36 min/ 160%), as seen in Figure 8(b) and (c). This resulted in a warning time of 36 min with the brass blocks vs. 6 min with phenolic plates. This dataset provides empirical evidence to support the significant role that cell packaging & system engineering plays in determining the warning time.

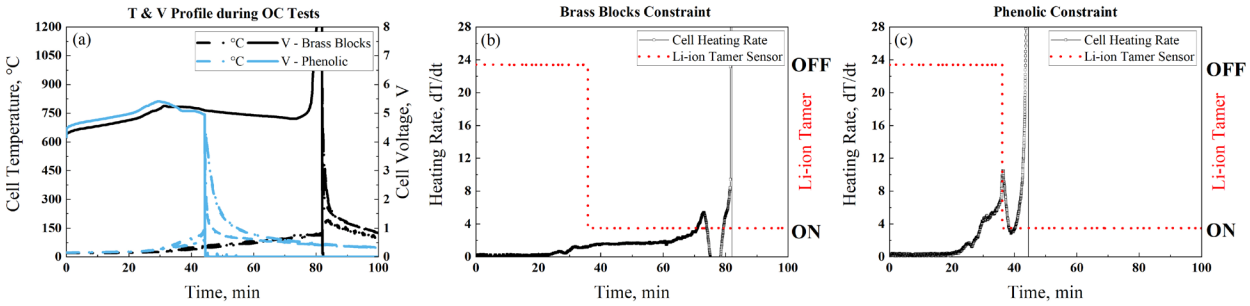

Figure 8. Evaluation of electrical failure behavior and VOC sensor triggering time for NMC cells constrained with brass blocks and phenolic plates: (a) voltage and temperature response during OC failure; (b) heating rate; and (c) sensor triggering time

Overtemperature Failure Initiation

Figure 9 through Figure 17 show the results of OT tests with three gas sensors (VOC, Combined Gas, H_2), gas evolution with FTIR/MS (only for single cells), rapid EIS (iRIS), and voltage and temperature measurements. The in-operando testing was accomplished by making measurements while the target cell was exposed to a 5 °C/min OT condition on one side of the cell until failure. Tests were performed for single cells, and 1s4p. The gas sensors path length was 22.9 cm away from the cell; the path length of the FTIR and MS was on the order of 10s of feet. The response time of the FTIR and MS will be slightly delayed relative to the sensor in part due to the difference in path length, although this delay is relatively minimal (<30 seconds).

Overtemperature Failure in Single Cells

The voltage and temperature during OT testing are shown in Figure 9(a). The thermal runaway occurred at 181 °C, reaching maximum temperatures close to 1000 °C. As the cell reaches the onset to thermal runaway, there is minimal voltage loss. This level of heat and voltage fluctuation may be difficult to detect within a localized area of a battery pack. Temperature and voltage sensors in this work were not sensitive enough to detect minute fluctuations and/or did not use sufficient sampling rates due to the very high precision and short timescale required to detect changes in the cell voltage and temperature prior to thermal runaway. If the sampling frequency is too low, then quick changes in the voltage could easily be missed. Figure 10 is an expanded view of the voltage differential of the cell tested in Figure 9. The only changes identified were those attributed to a voltage perturbation from rapid EIS measurements, and not associated with the heated cell. The voltage perturbations associated with the rapid EIS became more prominent as the severity of the abuse conditions increased. This is attributed to an increased cell internal resistance, resulting in substantial voltage polarization towards the end of the test.

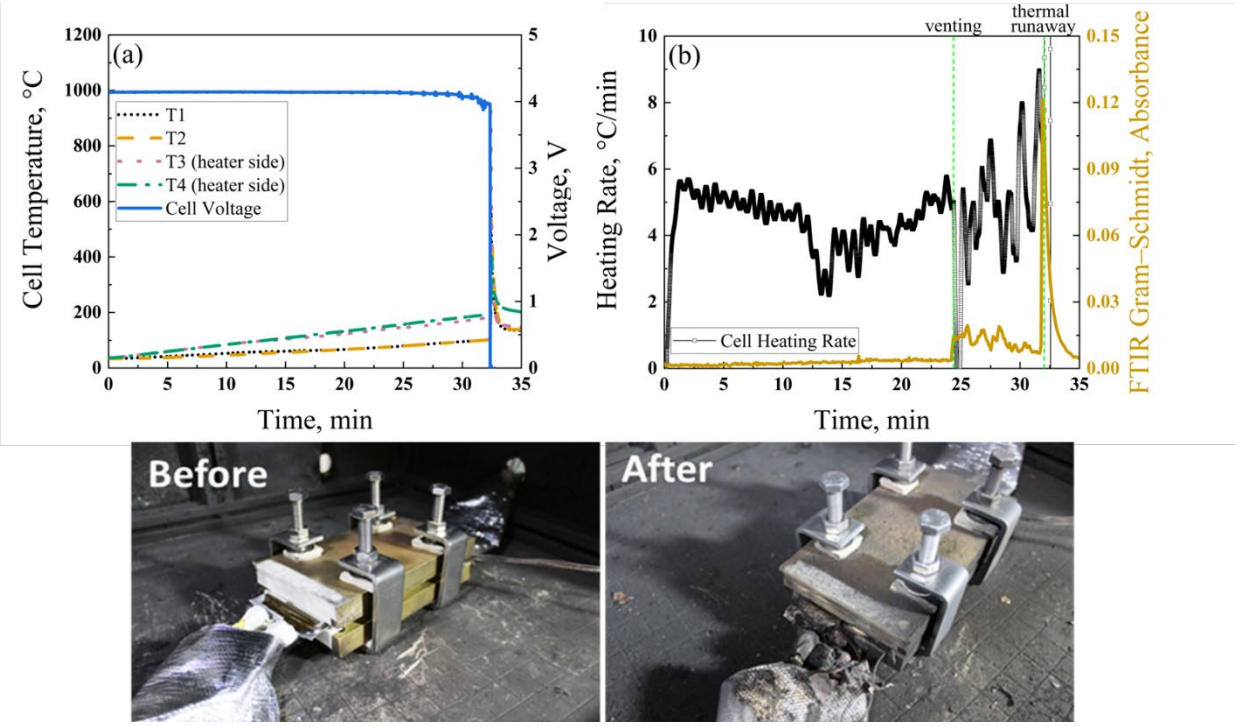

Figure 9. (a) Temperature and voltage response of a single 11.6 Ah NMC cell during an overtemperature test, (b) heating rate and time resolved FTIR measurements and (c), before and (d) after failure test images

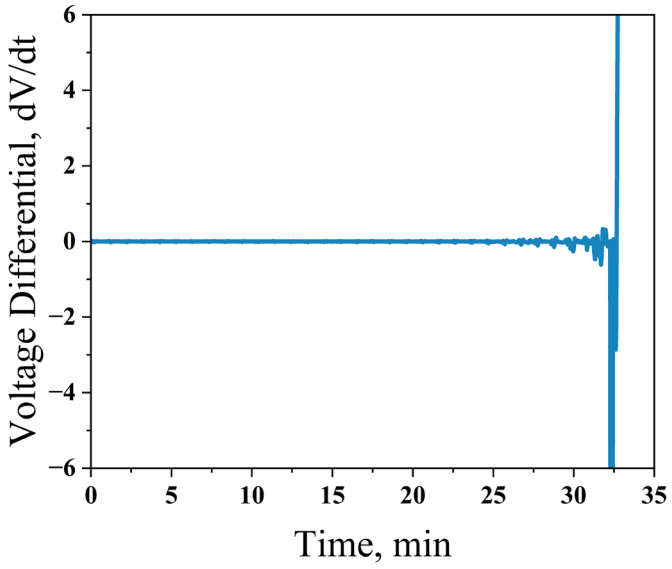

Figure 10. Voltage differential during the OT test in Figure 9 show only perturbations due to rapid EIS measurements with no indications of damage to the cell.

Time-resolved FTIR measurements were conducted during the test to correlate the results to those obtained with commercially available gas sensors. The results are presented in Figure 9(b),

in which the heating rate was overlayed with the FTIR Gram Schmidt spectra to identify the point during the OT test at which vented gases were detected. The first signal related to gas generation due to electrolyte decomposition (see Figure 11) was identified slightly before venting was observable from heating rate measurements, with FTIR showing a $\Delta t_{warning\ time}$ of 7.8 min.

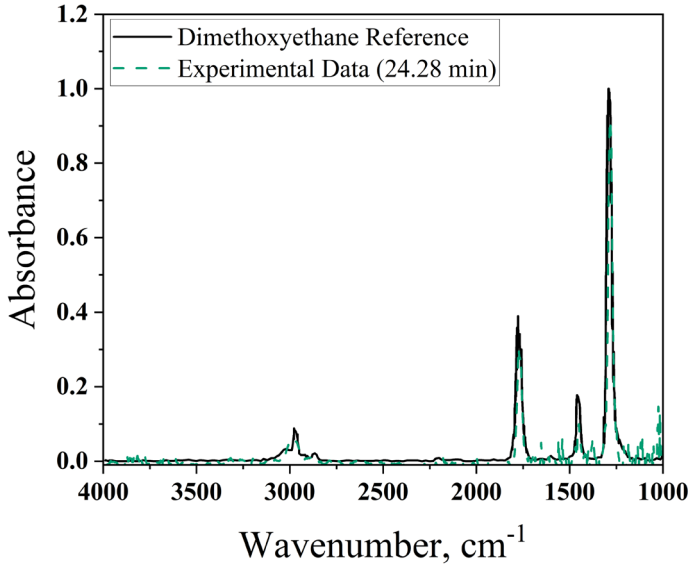

Figure 11. FTIR absorbance spectra at 24.28 min of the single cell subjected to overtemperature testing

A signal related to gas generation was collected 24.28 minutes after the single cell OT test was initiated. This signal is associated with the generation of gas resulting from electrolyte decomposition, as substantiated by the correlation of the data with dimethoxyethane (DME) electrolyte solvent through data analysis and fitting with the OMNIC SPECTA library as seen in Figure 11. The FTIR signal was detected slightly before venting was noted on the heating rate measurement.

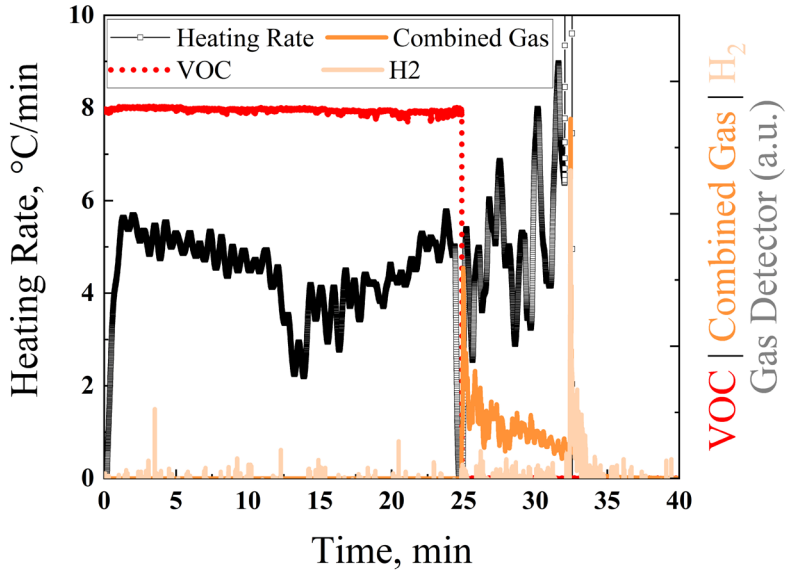

Figure 12. Commercial gas sensors response during overtemperature test of an 11.6 Ah pouch cell

The response of commercially available gas sensors is shown in Figure 12. The VOC and Combined Gas sensor, which both detect VOCs, triggered during cell venting, providing a $\Delta t_{warning\ time}$ of 7.1 min. The hydrocarbons detected by these two sensors are generated from the evaporation and decomposition of organic electrolyte solvents and carbon-containing components at temperatures <160 °C (Cai et al., 2021; Fernandes, et al., 2018; Jia et al., 2022; Shen et al., 2023; Zhang et al., 2022). This was confirmed with the MS measurements shown in Figure 13, where multiple hydrocarbons were detected during thermal decomposition of the electrolyte and electrodes. Hydrocarbons such as ethane (C_2H_6), and ethylene (C_2H_4) were identified during cell venting along with gases produced by the degradation of other organic components such as methane (CH_4). However, hydrogen (H_2) was not detected during venting because hydrogen generation typically occurs during major cathode decomposition at much higher temperatures (~200 °C) (Golubkov et al., 2014; Cai et al., 2021; Fernandes, et al., 2018; Jia et al., 2022; Shen et al., 2023; Zhang et al., 2022). This resulted in a generally shorter warning time for H_2 based sensors compared to VOC sensors. For this test, MS detected hydrogen <1 min prior to thermal runaway, compared to the ~7-minute warning from the VOC and Combined Gas sensors (Huang et al., 2022; Metzger et al., 2016; Tang et al., 2021; Zhang et al., 2014). The H_2 sensor triggered nearly at the onset of thermal runaway, leaving a very short response time. The later detection with the H_2 sensor vs. the VOC sensor may also be due to the higher trigger threshold (ppm vs. ppb).

The heating rate measured by a TC is dependent on events within the cell that can affect heat transfer properties. Drops in heating rate, e.g., those occurring between 12.5 and 15 minutes in Figure 12, can be a result of gas production creating separation between the cell casing material and the cell stack. This could temporarily reduce the heat transfer from the cell stack to the location of the TC. At ~25 minutes, the sharp drop-in heating rate is due to the cooling effect from cell venting.

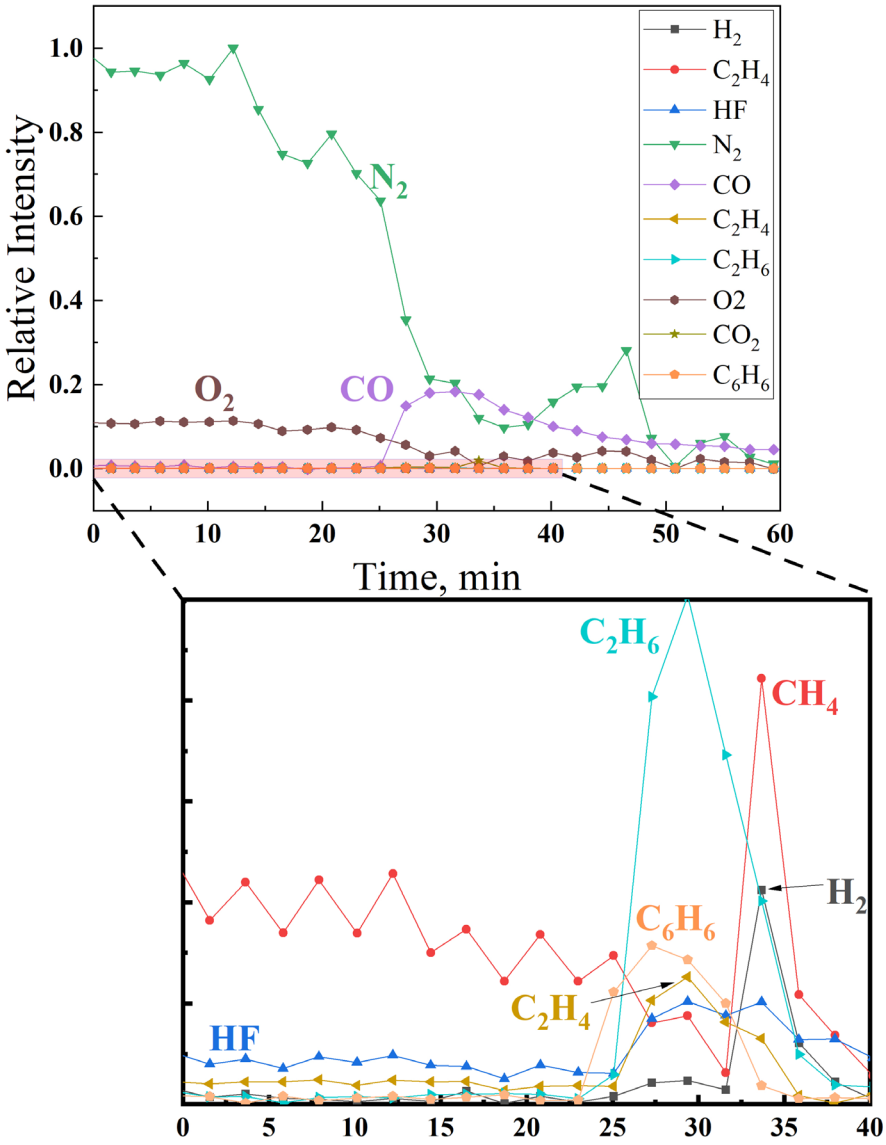

Figure 13. Time-resolved mass spectrometry during overtemperature test of a 11.6 Ah pouch cell

This cell testing was coupled with electrochemical diagnostics in the form of rapid EIS (0.1 Hz – 1638 Hz). As cells are subjected to abuse conditions, the cell temperature increases, resulting in a temporary reduction in cell internal resistance due to more favorable kinetics and a higher ionic conductivity at elevated temperatures. This minimum value for a representative impedance response is illustrated with a red open star in Figure 14(a). At that point, the cell materials begin degrading as this temperature (~100°C) is consistent with the degradation and reformation of solid electrolyte interphase, leading to an increase in cell resistance and subsequent increase in the magnitude of the impedance (Dong et al., 2021; Lyu et al., 2022; Feng et al., 2018). This increase after a minimum (local minima) was taken as a marker for failure warning, represented with a solid blue star in Figure 14(a). Figure 14(b) illustrates the magnitude of the impedance at 0.1 Hz extracted from full spectrums of rapid EIS measurements (0.1 Hz – 1638 Hz). These rapid EIS measurements were performed every 60 seconds during the single cell OT test. For single cell testing, changes in cell impedance are easier to detect allowing for a coarser sampling

rate. At lower frequencies (<1kHz), where processes govern charge transfer and diffusion, significant changes were identified. For the sake of time-resolved data representation, the magnitude of the 0.1 Hz frequency response is shown for time resolved plots, but full spectrum EIS data was gathered at each time stamp (Figure 15). The failure marker was found at about 82 °C, which gave a warning time of 22.5 min. When examining the full spectrum, the data clearly showed the charge transfer semi-circle and diffusion tail up to the magnitude minimum. However, one minute later, during the failure marker, the Nyquist plot appears as a linear line. It is also worth noting that the failure marker location of 82 °C is close to the temperature of SEI degradation, which is often the initial self-heating reaction in Li-ion thermal runaway (Feng et al., 2018; Andersson et al., 201999; Gao et al., 2023; Haik et al., 2011; Jiang et al., 2004; Liu et al., 2021).

In scenarios of excessive temperature leading to failure of single cells, the use of rapid EIS showed a distinct advantage over gas sensors for early detection. Specifically, rapid EIS was able to identify a malfunctioning cell with a significantly larger warning time (>3 times longer), thereby allowing for earlier response times to potentially intervene and mitigate further damage.

Yet, this could be challenging in battery packs where multiple cells are connected in series and/or parallel configurations. The interdependence of cells within a pack can mask symptoms of failure, making it difficult to isolate and diagnose problematic cells. Therefore, understanding the limitations of these diagnostics (commercial gas sensors and rapid EIS) during OT testing as size scales from single cells to a larger pack (1s4p and 2s4p in this work) is critical but beyond the scope of this work.

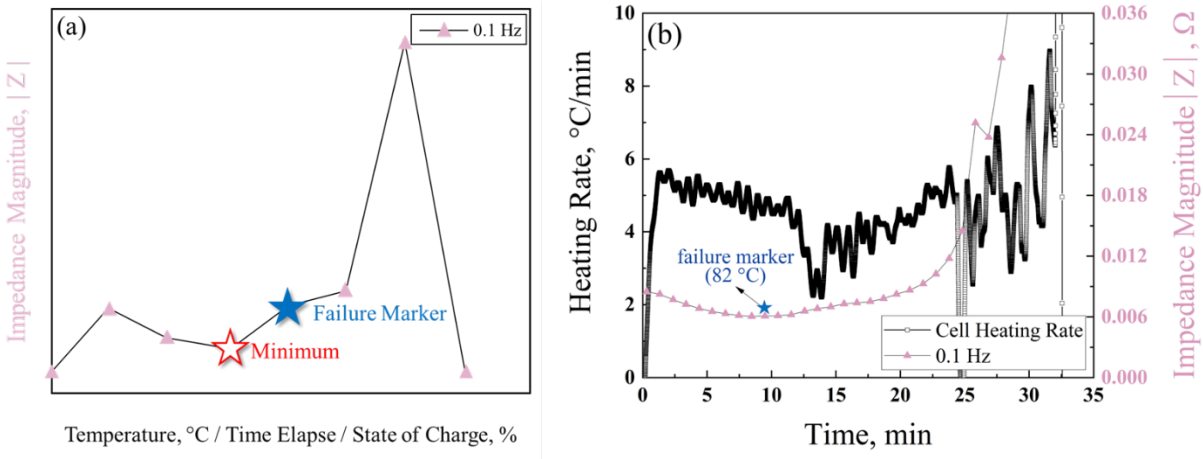

Figure 14. (a) Qualitative graphical representation of rapid EIS failure marker (solid blue star) during abusive conditions, and (b) rapid EIS response during OT test of a 11.6 Ah single pouch cell

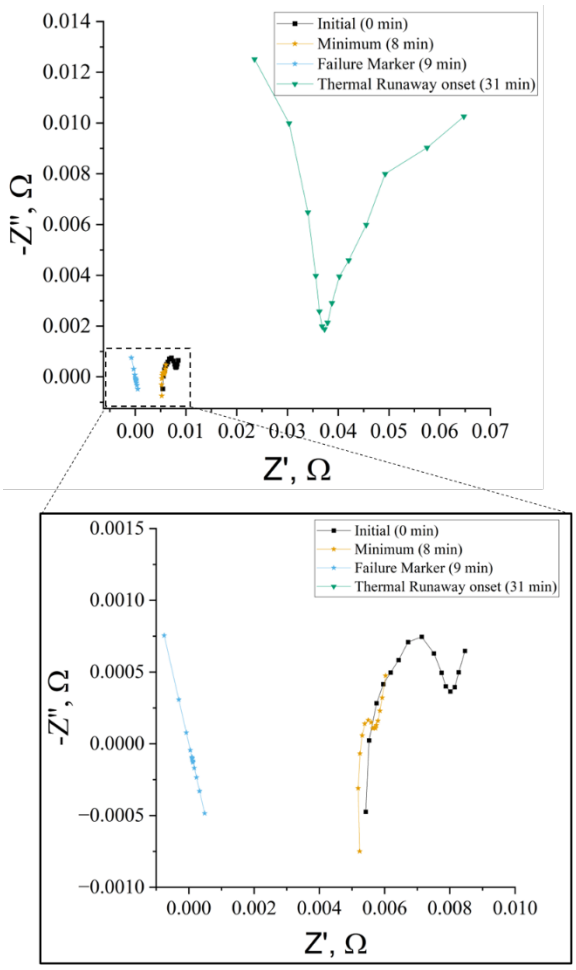

Figure 15. Full frequency spectrum Nyquist plots collected during the single cell overtemperature abuse test at the start of the test, the 0.1 Hz impedance magnitude minimum, the failure marker as defined in the main text, and onset of thermal runaway

Overtemperature Failure in a 1s4p Pack Configuration

Parallel strings of four cells were constructed using the same 11.6 Ah NMC pouch cells used in single cell testing. The string had a maximum operating voltage of 4.2 V and a nominal capacity of 46.4 Ah. The OT testing was performed by affixing brass plates to the pack and heating the edge cell of the string (cell 1) with two heat cartridges inserted into the plate. The pack diagram and image of the testing setup are presented in Figure 16. The gas sensors were situated at 22.9 cm from the battery pack, the voltage was measured at the pack level, and an impedance measurement of the entire 1s4p string was collected every 20 seconds throughout the duration of the test. The data collection rate needed for the 1s4p pack is three times finer than that of the single cell due to the ‘washing out’ of the signal of a single failing cell in the pack. The term 'washing out' refers to when the impedance signal becomes less distinct or disappears.

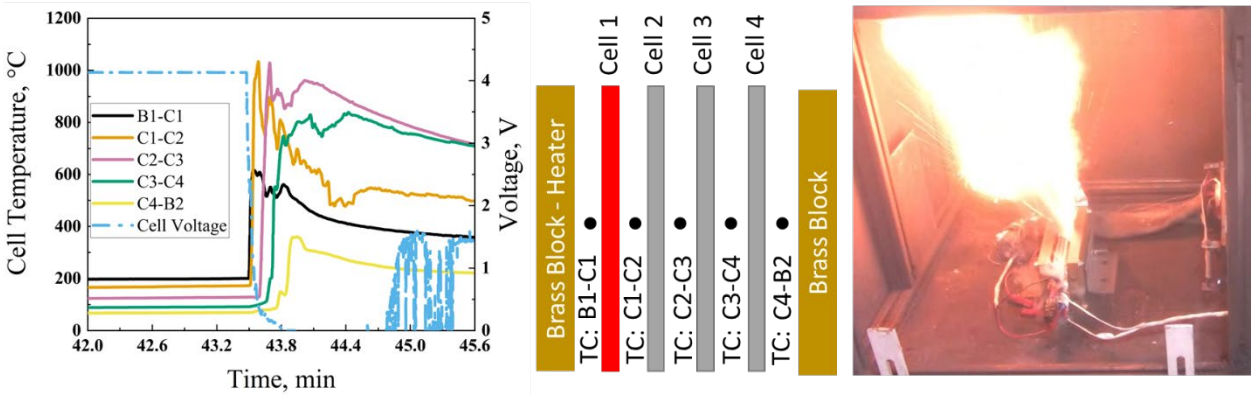

Figure 16. Temperature and voltage response of an overtemperature test of the edge cell within a 1s4p battery pack (left). The thermocouple map (middle) and thermal runaway video still (right) are also illustrated.

The temperature at which thermal runaway occurred for the triggered cell was 199 °C. Heat transfer to adjacent cells lead to preheating, resulting in an energetic thermal propagation throughout the stack. Temperatures reached up to 1,000 °C, consuming the entire pack within 15 seconds of cell 1 undergoing thermal runaway, as depicted from the temperature profile and video still in Figure 16. It is noteworthy that onset temperature was higher for the parallel string (199 °C) in comparison to the single cell (181 °C). For a single cell, the heat generated during failure is generally confined to an individual cell. However, in a multi-cell battery pack, increased heat transfer via adjacent cells or interconnections could result in a larger temperature variation. This can lead to a disparity in onset temperature between single cell and pack testing.

Figure 17(a) shows the gas sensors measurements on the 1s4p pack. The VOC and Combined Gas sensors triggered almost simultaneously during the initial off-gassing stage of cell 1. The H_2 gas sensor triggered during the later stage of thermal runaway. For this pack-level testing, $\Delta t_{warning\ time}$ was calculated based on TR_{time} of the targeted cell (cell 1). The VOC sensor and Combined Gas sensor provided a $\Delta t_{warning\ time}$ of 17.3 minutes. The H_2 sensor, however, failed to provide any warning time.

The increased $\Delta t_{warning\ time}$ of the VOC sensor and Combined Gas sensor (17.3 minutes) for the 1s4p pack vs. the single cell ($\Delta t_{warning\ time}$ 7.1 minutes) is attributed to increased heat transfer in the pack vs. the single cell, leading to a longer time between venting and thermal runaway. Both units—single cell and battery pack—experienced venting roughly at the same temperatures (144 to 152 °C). However, the pack experienced thermal runaway at a higher temperature (and thus a longer time after venting) due to more effective means of heat transfer out of the target cell.

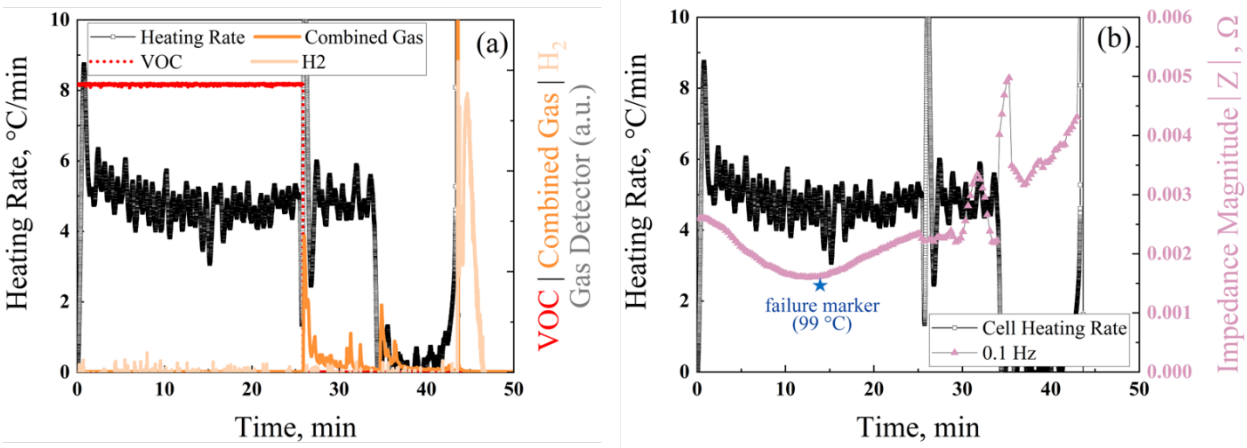

Figure 17. (a) Gas sensor and (b) rapid impedance spectroscopy measurements during an over temperature test of the edge cell within a 1s4p battery pack

For the sake of time-resolved data representation, the magnitude of the 0.1 Hz frequency response is shown for time resolved plots in Figure 17(b), but full spectrum EIS data was gathered at each time stamp (Figure 18). For the rapid EIS shown in Figure 17(b), the failure marker was identified at 99 °C after a subtle plateau at the minimum, providing a $\Delta t_{warning\ time}$ of 29.2 minutes. In general, electrochemical signatures possess the capability to identify earlier, crucial stages of degradation under abusive conditions. However, the equipment's sensitivity and ambient conditions will have a significant impact on the outcome. Furthermore, as the battery pack becomes more complex, the electrochemical signals tend to be "washed out", making it difficult to pinpoint critical thresholds. Particularly, it is possible that the impedance characteristics of individual cells may average out, or there may be electrical interference, wherein the more intricate the wiring and connections, the higher the number of false positives. This is evident when comparing the rapid EIS in Figure *14*(b) with Figure 17(b), where the delta between the minimum and the failure marker for the pack was more subtle (1.2×10^{-5} Ohms) compared to the single cell (2.6×10^{-5} Ohms). In addition, when examining the full spectrum EIS for this test, the loss of the clear charge transfer semi-circle and diffusion tail provides evidence of a 'washed out' effect for most frequencies, although the 0.1 Hz failure marker is still present.

The gas sensors and rapid EIS provided a failure marker at significantly different temperatures, 153 °C and 99 °C, respectively. Ideally, the failure marker should be identified at low temperatures as more exothermic self-heating reactions occur as temperatures increase >100 °C.[62] Detection at low temperatures could allow for early intervention, minimizing damage to the surrounding cells/packs and increasing the probability of successfully mitigating thermal runaway propagation. Although these diagnostics showed failure markers at temperatures >99 °C, the ability to intervene after identifying these markers was explored and discussed in section 3.5.1.

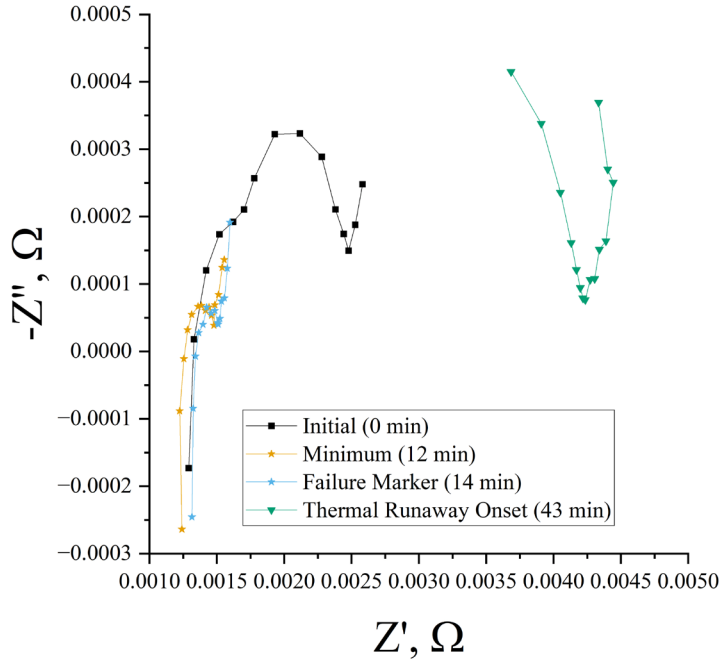

Figure 18. Full frequency spectrum Nyquist plots collected during the 1s4p overtemperature abuse test at the start of the test, the 0.1 Hz impedance magnitude minimum, the failure marker as defined in the main text, and onset of thermal runaway

Table 2 summarizes the key findings of the OT tests. The $\Delta t_{warning\ time}$ between single cells and a parallel string of cells varies significantly. This discrepancy is intricately linked to the specific design of the battery pack, where minor variations could influence how quickly failure markers are detected and addressed. One standout of the results is the superior performance of the rapid EIS as a diagnostic tool compared to commercial gas sensors. The impedance magnitude provides a substantially longer $\Delta t_{warning\ time}$, allowing for more proactive responses to thermal failures. However, while rapid EIS presents this clear advantage, implementing it for onboard diagnostics may pose certain challenges. These challenges could relate to integrating rapid EIS into existing diagnostics systems, the need for specialized equipment, or the requirement for more sophisticated algorithms to interpret impedance data accurately. However, several groups in industry and academia are actively working towards a solution to these challenges for standard EIS systems (Pastor-Fernandez et al., 2017; Wang et al., 2023).

Table 2. $\Delta t_{warning\ time}$ for single cell and pack level testing during over temperature conditions (single data points).

Cell Configuration	**Sensor**	**$\Delta t_{warning\ time}$ (min)**
Single cell	iRIS	22.5
	VOC	7.1
	Combined Gas	7.1
	H_2	-0.4
1s4p (OT of cell 1)	iRIS	29.2
	VOC	17.3
	Combined Gas	17.3
	H_2	-0.4

Overcharge Failure Initiation

Figure 19 through Figure 28 illustrates the outcomes of OC tests coupled with three gas sensors (VOC, Combined Gas, H_2), monitoring gas evolution through FTIR and MS (only for single cells), rapid EIS analysis (5% SOC intervals), and voltage and temperature measurements. The in-operando testing was accomplished by taking measurements while the target cell was exposed to OC conditions. Tests were performed for 11.6 Ah NMC/gr single cells, 1s4p packs, and 2s4p packs.

Overcharge Failure in Single Cells

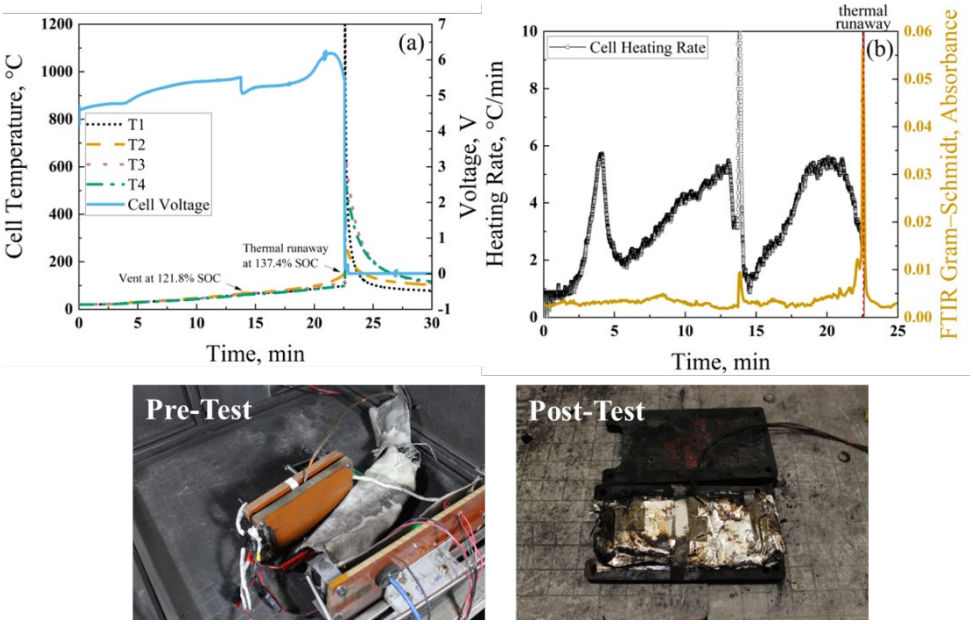

Figure 19. (a) Temperature and voltage response of a single 11.6 Ah NMC cell during overcharge conditions, (b) heating rate and time-resolved FTIR measurements, and (c), (d) pre and post failure test images

The temporal evolution of cell temperature and voltage can be observed in Figure 19. It is noteworthy that there is a minimal rise in temperature and a steady rise in voltage as the SOC reaches 123 percent. However, at this point, the voltage abruptly decreases, and the temperature surges more rapidly as it approaches the onset SOC to thermal runaway (137% SOC). This behavior could be attributed to a threshold where the delithiation of the NMC structure has reached a critical degradation point, which results in reactions with the electrolyte leading to gas generation.

Time-resolved FTIR spectroscopy in the form of Gram Schmidt is presented in Figure 19(b) with an overlay displaying the cell heating rate as a reference parameter. The initial detection of a signal occurred at a SOC of 122.8 percent when the cell vents. This occurred after the commencement of cell heating, around 13.5 minutes, providing a $\Delta t_{\text{warning time}}$ of 8.8 minutes. VOC and Combined Gas sensors, Figure 20, showed a quick response with the sensors triggering at 123 percent SOC, slightly after FTIR detection of organics. This coincides with the onset of rapid heating, as Figure 19(b) shows. Both commercial sensors provided 8.5 minutes $\Delta t_{\text{warning time}}$.

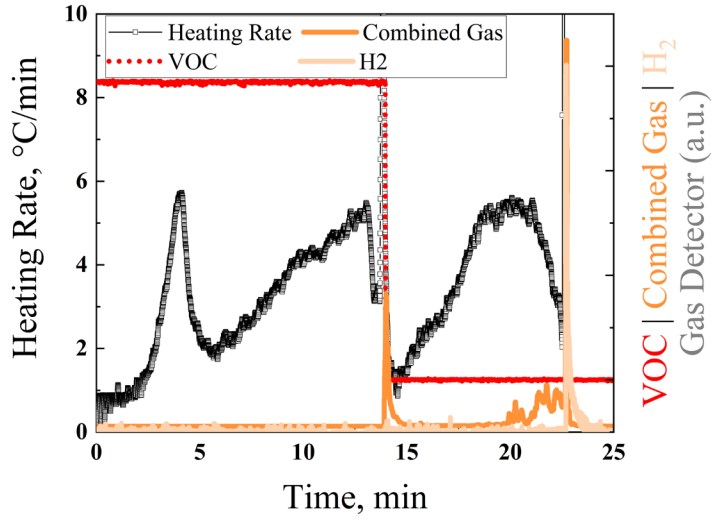

Figure 20. Gas sensor response during overcharge tests of a 11.6 Ah pouch cell

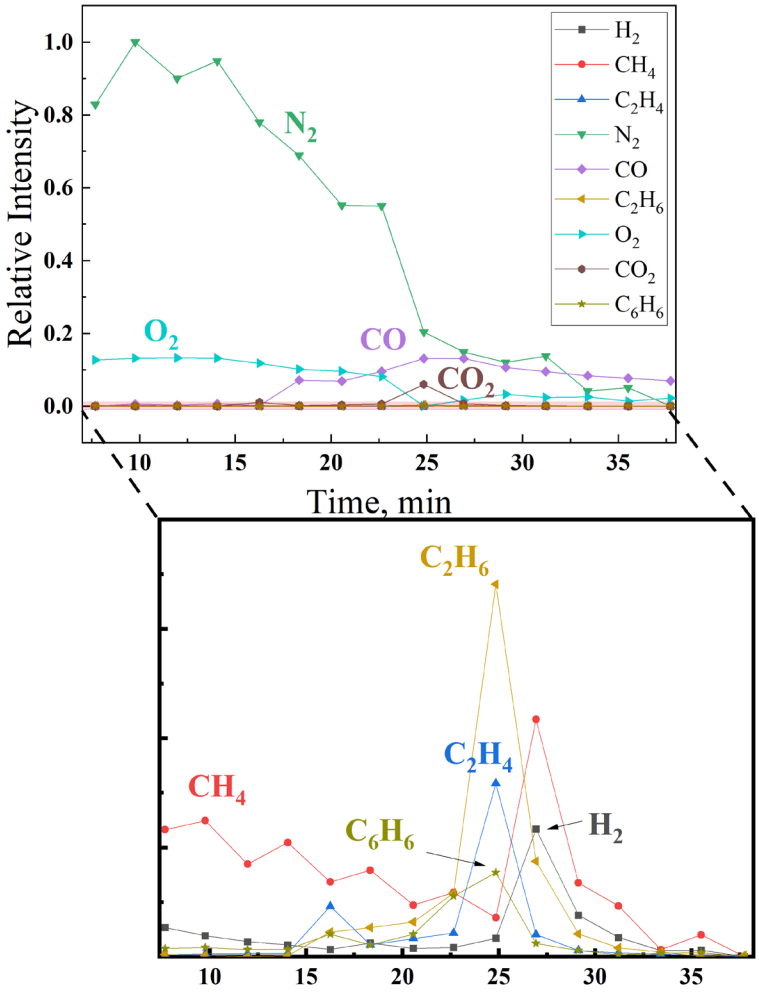

Figure 21. Time-resolved mass spectrometry collected during overcharge test of a 11.6 Ah pouch cell

During the OC test, gas measurements conducted with MS indicate a significant presence of carbon dioxide shortly after venting. However, most degradation byproducts from both the electrolyte and electrodes were detected following the initiation of thermal runaway, as depicted in Figure 21. An interesting observation is the disparity in the rate of gas generation between OC and OT failures. OC conditions result in electrochemical reactions and the breakdown of the electrolyte driven by the increasing voltage, leading to a more gradual release of gases. In contrast, in OT conditions, degradation and decomposition of components initiate at much lower temperatures, typically between 60 and 80 °C. This results in a distinct gas generation pattern that is characterized by rapid and frequently more aggressive gas emissions. Figure 22 shows the impedance magnitude response of the 0.1 Hz frequency during the OC test. When selecting a failure marker during OC tests, the rapid EIS measurement at 100 percent SOC was not considered, since the impedance at that stage would be heavily connected to the transition from no load to active load. Therefore, an indicator of imminent failure was discernible at a SOC of 125 percent. This failure marker provided a $\Delta t_{\text{warning time}}$ of approximately 7.4 minutes. Full spectrum EIS data presented in Figure 23 showed that the charge transfer semi-circle elongates during the failure marker, as the impedance for further cathode delithiation continues to increase.

In the context of early failure detection during OC conditions, the data indicates that rapid EIS exhibits a shorter warning time compared to the VOC or Combined Gas sensors. While the comparative advantage of rapid EIS is evident in the earlier warning time it provides during OT tests, this is not necessarily true for the OC tests presented in this work. The impedance response reflects what is occurring electrochemically within a cell (change in resistance due to factors such as SEI, electrolyte loss, poor charge transfer, etc.) while the gas sensors reflect gas generation within the cell (material decomposition) after breaching the cell casing. During OC, the timing of electrochemical resistance build up and material degradation are much closer together with venting occurring before a noticeable change in the impedance. This contrasts with the OT abuse test where a change in the impedance is seen far in advance of the cell venting. It is beyond the scope of this work to identify the cause of this difference.

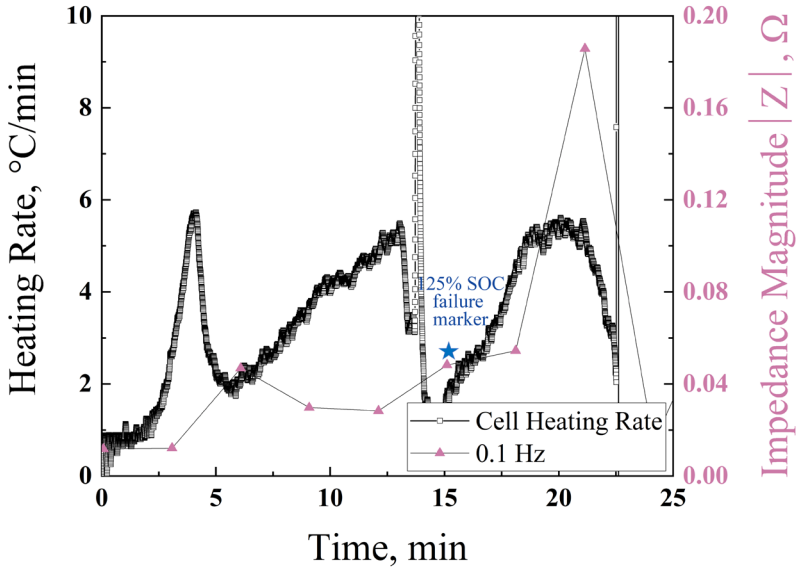

Figure 22. Rapid EIS response during overcharge test of an 11.6 Ah pouch cell

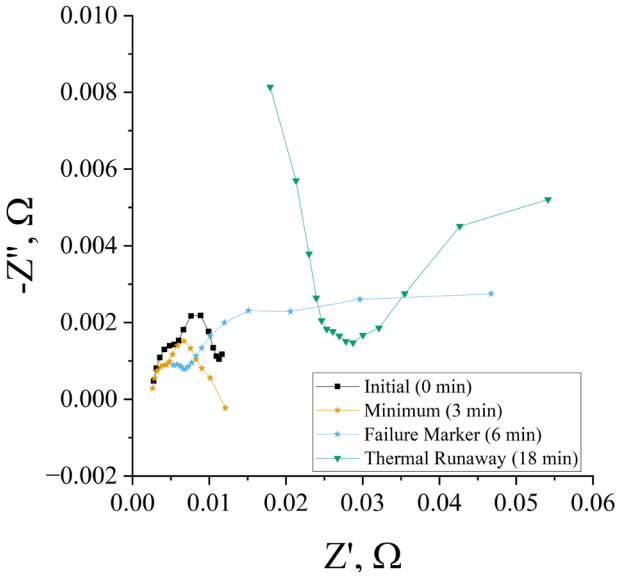

Figure 23. Full frequency spectrum Nyquist plots collected during the single cell overcharge abuse test at the start of the test, the 0.1 Hz impedance magnitude minimum, the failure marker as defined in the main text, and thermal runaway

1s4p Overcharge Failure in a 1s4p Pack Configuration

OC testing of the 1s4p configuration was conducted at a constant current rate of 1C (46.4 A), while adhering to a compliance voltage of 20 V. The thermal and voltage behaviors (measured at the pack level) of the pack are elucidated in Figure 24, which also includes a schematic representation of the unit under investigation and a photograph of the experimental setup. The TC situated between cells 2 and 3 registered a rapid increase in temperature, indicative of the initiation of thermal runaway and a battery fire within one of the central cells.

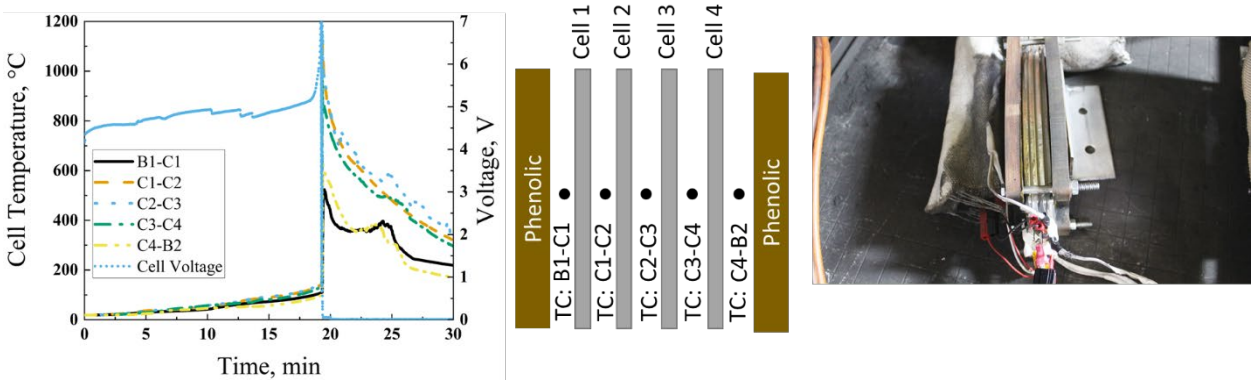

Figure 24. Temperature and voltage response during overcharge of a 1s4p battery pack (left). A schematic representation of the unit under investigation (middle) and test setup photograph (right) are also included.

These cells are subject to more severe conditions due to three factors: 1) internal heating from OC abuse, 2) heat contributions from adjacent cells, and 3) reduced convective heat transfer to the environment due to no contact with fixturing plates. This cumulative impact mitigates any source of heat dissipation and ultimately exacerbates thermal runaway, leading to higher maximum temperatures. The cells within the center of the pack reached temperatures above the capability of the TCs (>1200 °C), while the edge cells' temperature ranged between 523 °C and 1110 °C. This highlights that the geometric location within the pack significantly effects the cells' abuse response. While peripheral cells can readily dissipate heat due to conduction to the fixturing assembly or the proximity of dedicated cooling systems, central cells are comparatively isolated.

Thermal runaway onset occurred at 132 percent SOC, determined by the time when cell 2 failed and initiated thermal propagation. Within 3 seconds, the heat released by cell 2 transferred into neighboring cells, setting in motion an energetic thermal propagation sequence throughout the battery pack until all 4 cells were in thermal runaway. Figure 25(a) illustrates that the VOC sensor and Combined Gas sensor triggered during the initial off gassing phase of the battery pack, with the VOC sensor ($\Delta t_{warning\ time}$ of 8.5 min) triggering seconds after the Combined Gas sensor ($\Delta t_{warning\ time}$ of 8.6 min). In contrast, the H_2 sensor triggered a few seconds prior to the onset of thermal runaway, with a $\Delta t_{warning\ time}$ of 0.1 min. The warning times between the single cell and the 1s4p pack were within the same range, as detailed in Table 3.

Figure 25(b) serves as a visual representation of the impedance magnitude during OC conditions of the 1s4p configuration. At a SOC of 121 percent, a failure marker was detected, providing a 6.8-minute warning window before potential issues escalate further. The full spectrum EIS in Figure 26 exhibited the same elongation of the charge transfer semi-circle as seen with the single cell. However, compared to single cells, the failure marker was identified at a lower %SOC, yet the onset to thermal runaway was at a lower %SOC leading to a shorter $\Delta t_{warning\ time}$ for the 1s4p pack. These discrepancies in $\Delta t_{warning\ time}$ are not solely due to configuration but also stem from the intricacies of battery behavior. As batteries become more complex, such as in the 1s4p pack, the impedance signal tends to become less distinct, making it challenging to detect potential safety issues.

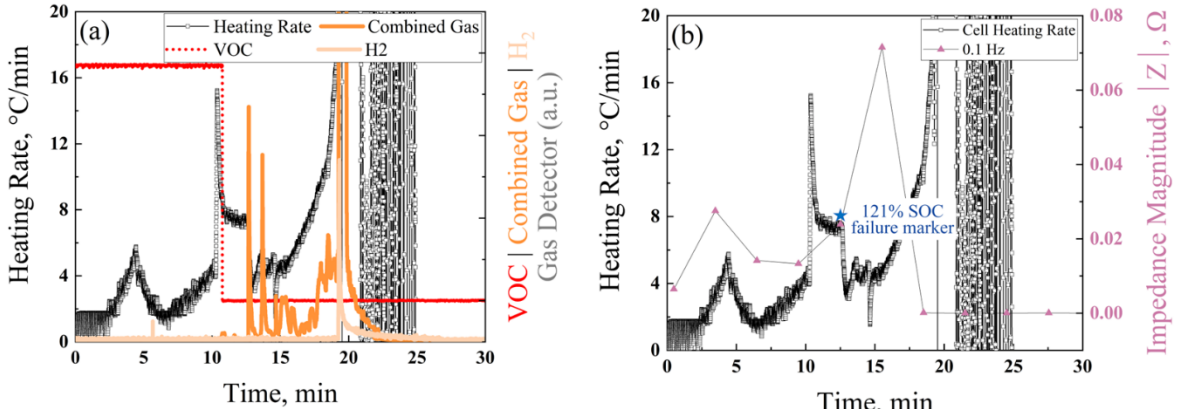

Figure 25. (a) Gas sensor and (b) rapid impedance spectroscopy measurements during overcharge failure of a 1s4p battery pack

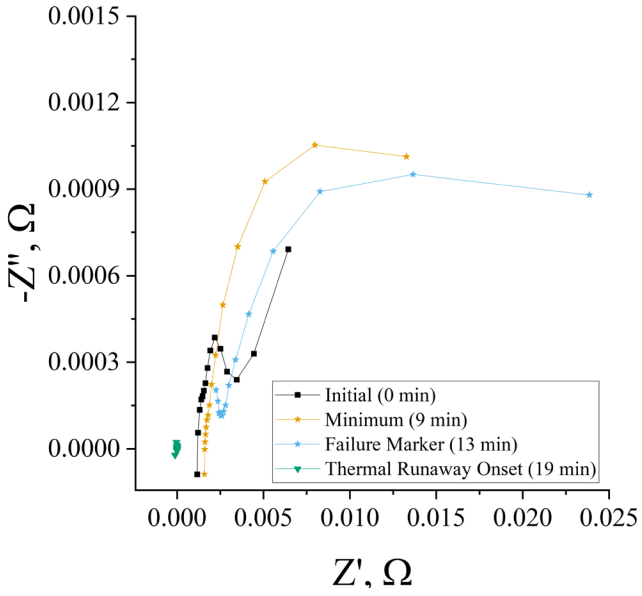

Figure 26. Full frequency spectrum Nyquist plots collected during the 1s4p cell overcharge abuse test at the start of the test, the 0.1 Hz impedance magnitude minimum, the failure marker as defined in the main text, and thermal runaway

Table 3. $\Delta t_{warning\ time}$ for 11.6Ah NMC pouch cells during OC conditions: cell and pack level testing (single data points)

Cell Configuration	Sensor	$\Delta t_{warning\ time}$ (min)	Sensor Triggered SOC (%)	Sensor Triggered T (°C)
Single cell	Combined Gas	8.6	123.0	67
	VOC	8.5	123.2	67
	iRIS	7.4	125.0	69
	H_2	-0.2	137.7	640
1s4p (pack OC - statistics based on cell 2 data)	Combined Gas	8.7	117.6	55
	VOC	8.5	117.9	55
	iRIS	6.8	120.8	65
	H_2	0.1	132.0	126
2s4p (OC of 1s4p string – statistics based on cell 8 data)	Combined Gas	6.5	118.7	86
	VOC	6.3	119.0	90
	iRIS	5.8	119.8	139
	H_2	0.4	128.8	84

Overcharge Failure in a 2s4p Pack Configuration

To understand the limitations of the diagnostic devices as the energy density increases and the pack design becomes more complex, the failure of a 2s4p battery pack was analyzed. The maximum operating voltage of the pack was 8.4 V and the maximum capacity was 46.4 Ah. The OC testing was performed on a 1s4p string within the 2s4p configuration by using a constant current of 1C (46.4 A) with a compliance voltage of 40 V. The OC tests were coupled with gas sensors and in-operando impedance monitoring of the whole 2s4p pack, during the continuously applied abusive condition.

The onset SOC to thermal runaway for the failed module in the 2s4p pack was 129 percent SOC. The heat from cell 8 dissipated to adjacent cells, resulting in an energetic thermal propagation through the stack reaching temperatures >1,200°C and consuming the whole pack in about 37 seconds, as can be seen in Figure 27. According to Figure 28(a), the VOC and Combined Gas sensors triggered at approximately the same time during initial off-gassing of the pack (warning times of 6.3 min and 6.5 min, respectively) while the H_2 sensor triggered during thermal runaway with a $\Delta t_{warning\ time}$ of 0.4 minutes. For the 2s4p pack, the $\Delta t_{warning\ time}$ with the gas sensors was shorter compared to the 1s4p test discussed in the previous section. The magnitude of the impedance for the 2s4p pack during OC is presented in Figure 28(b). The failure marker was identified at 120 percent SOC, with a warning time of 5.8 minutes. Full spectrum EIS behavior is presented in Figure 29.

The OC tests demonstrate that as the complexity of the battery and stored energy increases, the impedance signal starts to ‘wash out’, leading to shorter warning times. In addition, moving from a 1s4p configuration to a 2s4p configuration resulted in a warning time reduction for the gas sensors. The key findings of the OC tests, including the warning time, are summarized in Table 3 above.

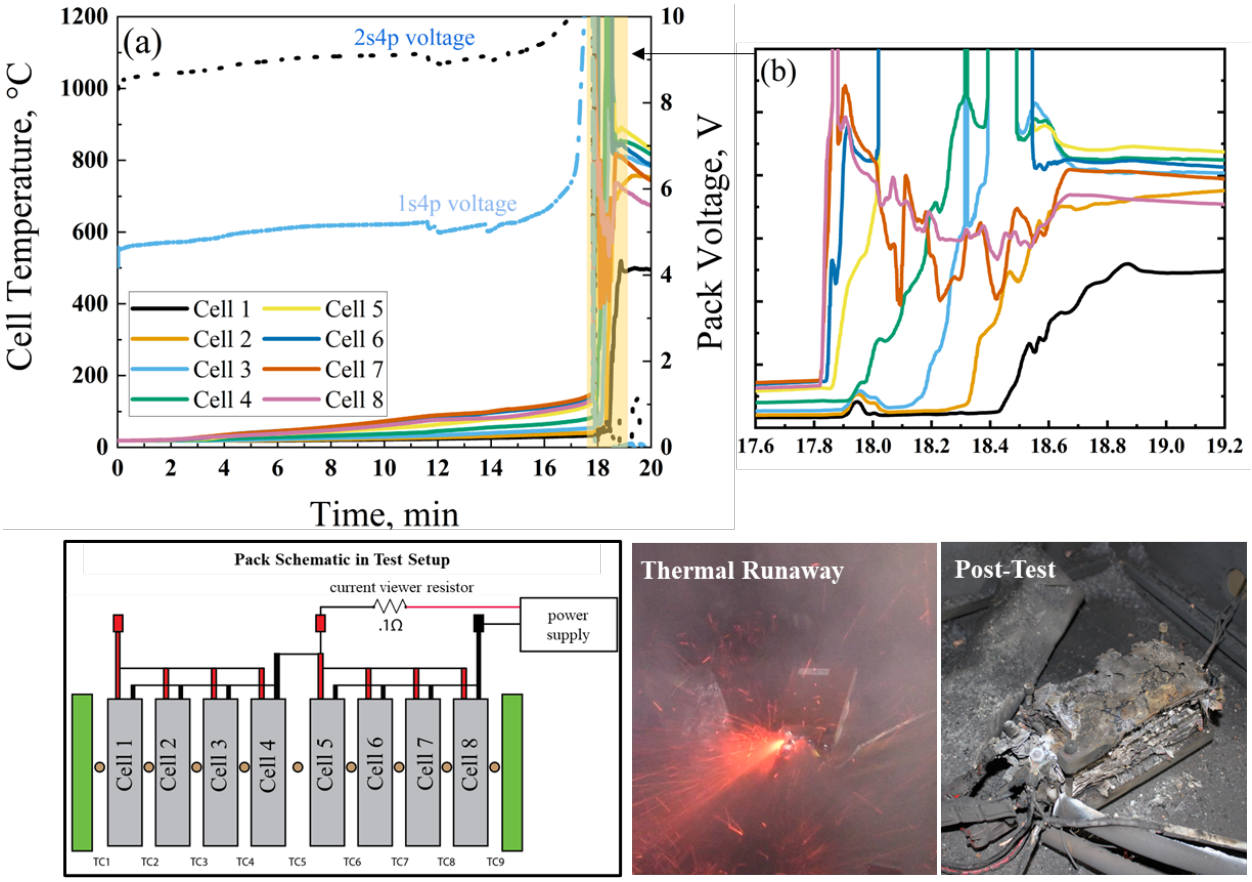

Figure 27. (a) Temperature and voltage response during overcharge of a 2s4p battery pack, and (b) zoomed-in section of panel (a). (c) A schematic representation of the unit under investigation and (d) during/post-tests photographs

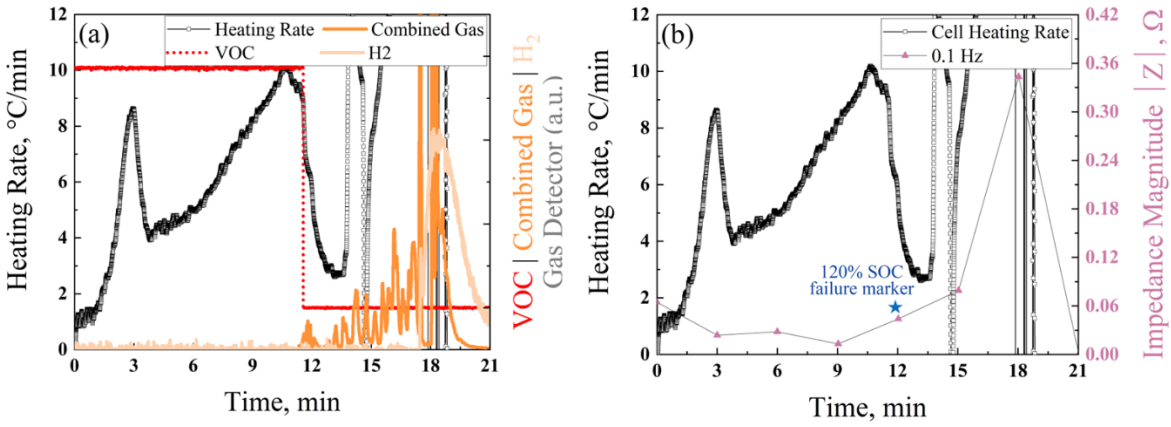

Figure 28. (a) Gas sensor and (b) rapid impedance spectroscopy measurements during overcharge failure of a 2s4p battery pack

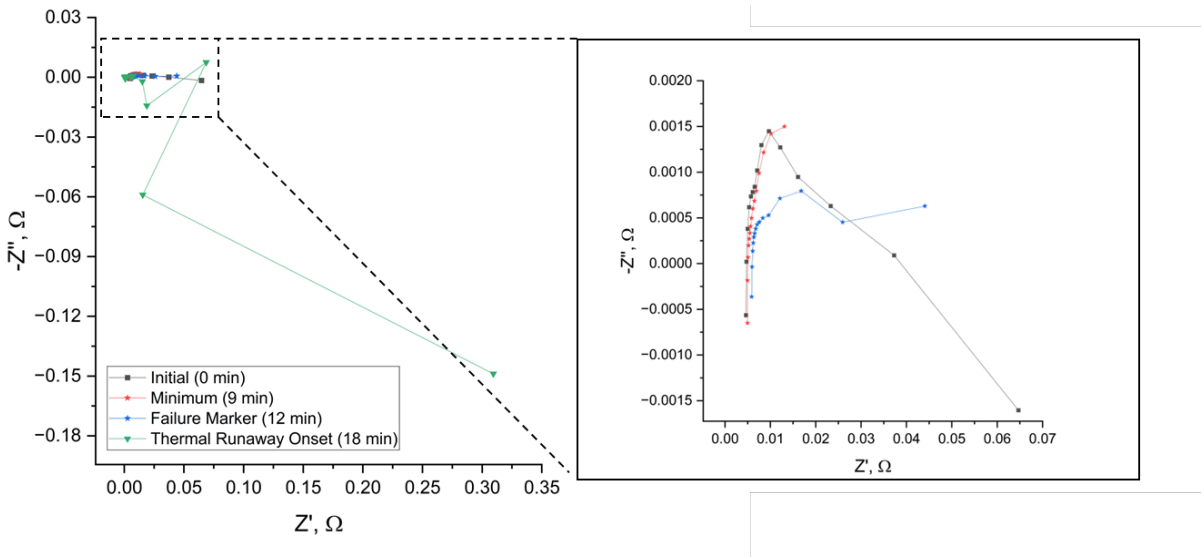

Figure 29. Full frequency spectrum Nyquist plots collected during the 2s4p cell overcharge abuse test at the start of the test, the 0.1 Hz impedance magnitude minimum, the failure marker as defined in the main text, and thermal runaway

Intervention at Identified Failure Markers

Overtemperature Failure Intervention

This work indicates that gas sensors and rapid EIS are viable candidates for the early detection of thermal runaway. When examined at both the individual cell and 1s4p array levels for OT abuse, the impedance magnitude offered an extended early warning timeframe relative to gas sensors, as seen in Table 2. This raises the critical question: are such warning times sufficient to allow for mitigation or prevent thermal runaway? To address this question, an OT experiment was executed using the same parameters and conditions as those outlined in the previous OT tests. As a proxy thermal mitigation strategy (Sun et al., 2022; Patil et al., 2021; Yuan et al., 2019), the heating element was deactivated upon either the triggering of the gas sensor or the identification of a failure marker through impedance magnitude. The deactivation of the heating element had the intentional effect of cooling the pack by convectively transferring heat to cooler surroundings, which in this case was simple ambient air.

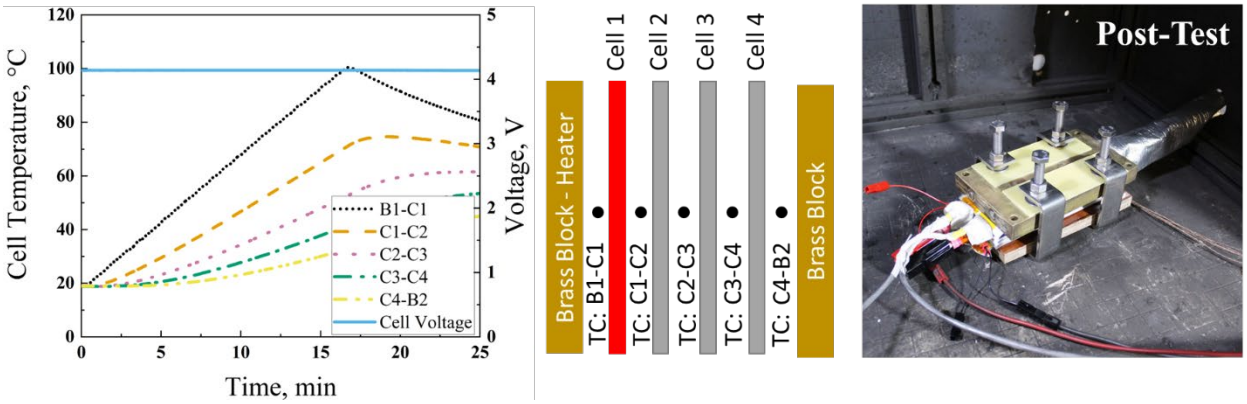

Figure 30. Voltage and temperature response of a 1s4p battery pack during overtemperature test (left). The thermocouple array (middle) and tests setup images (right) are also presented. In this test, the heating element was deactivated when a failure marker was identified.

In Figure 30, the voltage and temperature profile of the 1s4p intervention experiment is presented, revealing a spatially dependent heating rate ranging between 3 and 7 °C/min. The triggered cell reached a maximum temperature of 100 °C by the time the failure marker in the magnitude of the impedance (measured for the 1s4p string) was detected, as seen in Figure 31(b). Subsequent rapid deactivation of the heating element, led to a decrease in cell temperature, thereby averting thermal runaway. The gas sensors, shown in Figure 31(a), remained inactive throughout the experiment, as cell venting did not occur. No change in the pack voltage was observed during the test.

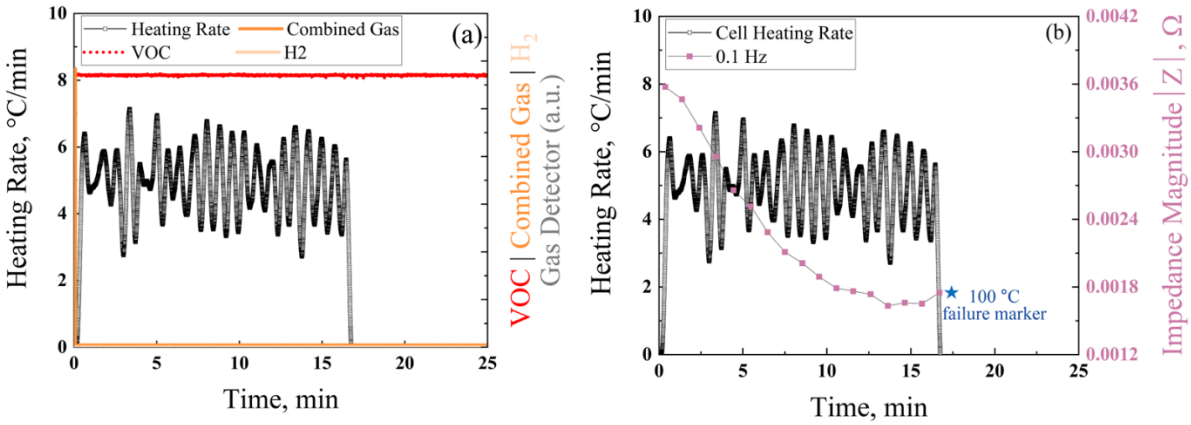

Figure 31. In-operando diagnostics measurements during overtemperature failure of a 1s4p battery pack:(a) COTs gas sensors, and (b) rapid EIS

Overcharge Failure Intervention

Building on previous tests, the effectiveness of early warning mechanisms during instances of battery overcharging was evaluated. Specifically, the study assessed whether these advance warnings are timely enough to either completely halt the onset of thermal runaway or at least reduce the likelihood of thermal propagation. To maintain a consistent experimental framework, an OC experiment following the same parameters and conditions specified in the earlier section on 1s4p battery overcharging was conducted. In this experiment, the procedure was designed to immediately cease the flow of electrical current to the battery if the gas sensors activated or if there was a discernible change in the impedance magnitude that typically signifies a failure (Sun et al., 2022; Olabi et al., 2022). This simulated the process of identifying a failure marker and subsequently shutting down the system.

Figure 32(a) presents a comprehensive overview of the voltage and temperature obtained from the 1s4p intervention experiment. The figure reveals that the temperature response is not uniform across the system but varies depending on the location. The center cells experienced a rapid increase in temperature, reaching a maximum of 54°C. The Combined Gas sensor then detected off gassing (Figure 32(b)) and the applied current was terminated. After the current was discontinued, a cooling trend was observed without any thermal runaway. The VOC sensor activated 35 seconds after the Combined Gas sensor during cell off-gassing. The H_2 sensor and rapid EIS (Figure 33) methods failed to identify any irregularities or abnormal behavior. It iw worth noting that the impedance magnitude does decrease with increasing temperature consistent with previous test, but no further increase in the impedance magnitude is seen prior activation of the VOC gas sensor.

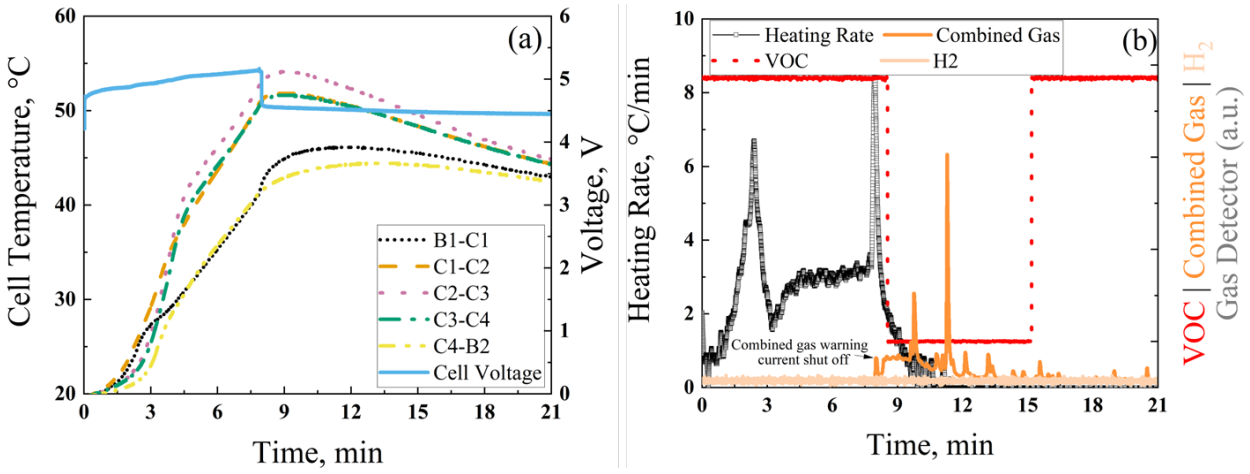

Figure 32. Intervention based on diagnostics response during overcharge of a 1s4p battery pack. (a) Voltage and temperature profile, and (b) COTs gas sensors measurements

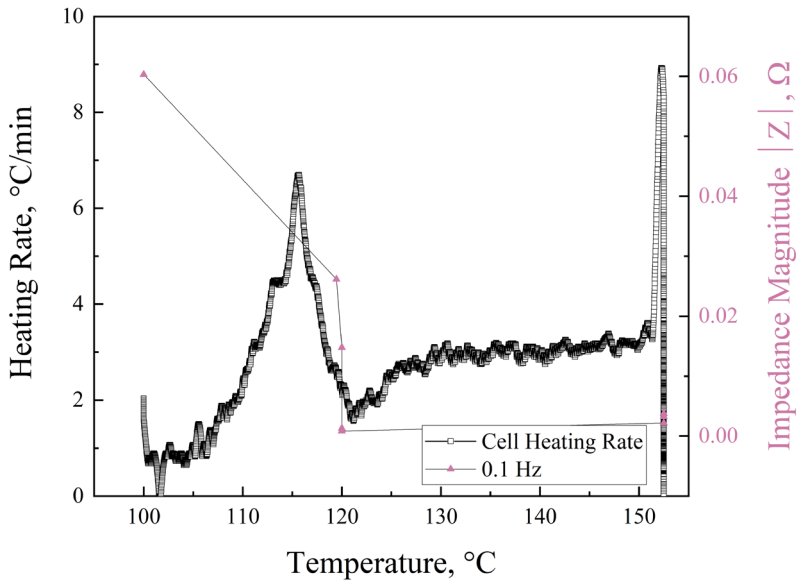

Figure 33. The time-resolved magnitude of impedance at 0.1 Hz for the 1s4p intervention test

This page is intentionally left blank.

Conclusions

Li-ion battery diagnostic sensors have been evaluated as tools for early warning detection of thermal runaway for cells and small packs. However, there remains a need for deeper comprehension and quantification of the warning time and effectiveness for on-board diagnostics when applied in EVs, including larger packs and higher voltage. Evaluation of the warning times during OT and OC tests demonstrated that rapid EIS consistently showed an earlier warning for the OT tests compared to gas sensors. For the OC tests, an earlier warning was observed with the VOC gas sensors. In the OT and OC tests, the H_2 sensors had the shortest warning time. In the OC tests, the warning time of rapid EIS was comparable to the VOC gas sensors. While rapid EIS does give the longest warning time in the OT tests, with the failure marker often appearing before the cell vents, the ability of picking up impedance changes in single cells within a pack decreases as the packs become larger. VOC sensors consistently triggered during cell venting, even in larger packs, in response to volatilized electrolyte solvent. However, thermal runaway mitigation strategies are most effective if used prior to cell venting. In many cases, the H_2 sensor did not trigger until after thermal runaway began. Due to the different response of the VOC gas sensors and the rapid EIS during OT and OC, a combination of both techniques is ideal for failure detection and mitigation.

Warning time can vary depending on multiple factors including cell type and abuse scenario. These could include the specific thermal properties of the battery pack, how closely packed the cells are, the efficiency of the thermal management system, and other design considerations. The measured warning times may be different to what was reported in this work for different cells/packs and different sensor implementation. The results of this work demonstrate that the ability and/or warning time of detection methods decreases as pack size increases.

An ideal BMS would incorporate rapid EIS, in combination with traditionally collected data points (i.e., voltage and temperature), to achieve detection of failure markers prior to venting. Gas sensors, such as the VOC sensor, would be incorporated to increase detection.

The work also demonstrates that cell failure management must include careful consideration of sensor application, and battery pack design. Evaluating this is essential for devising strategies that can enhance battery safety.

This page is intentionally left blank.

References

Abraham, D., Roth, E., Kostecki, R., McCarthy, K., MacLaren, S., & Doughty, D. (2006). Diagnostic examination of thermally abused high-power lithium-ion cells. *Journal of Power Sources*, *161*(1), 648–657. https://doi.org/10.1016/j.jpowsour.2006.04.088

Andersson, A. M., Edström, K., & Thomas, J. O. (1999). Characterisation of the ambient and elevated temperature performance of a graphite electrode. *Journal of Power Sources*, *81–82*, 8–12. https://doi.org/10.1016/s0378-7753(99)00185-8

Baakes, F., Lüthe, M., Gerasimov, M., Laue, V., Röder, F., Balbuena, P., & Krewer, U. (2022). Unveiling the interaction of reactions and phase transition during thermal abuse of Li-ion batteries. *Journal of Power Sources*, *522*, 230881. https://doi.org/10.1016/j.jpowsour.2021.230881

Balasingam, B., Ahmed, M., & Pattipati, K. (2020). Battery management systems—Challenges and some solutions. *Energies*, *13*(11), 2825. https://doi.org/10.3390/en13112825

Bates, A. M., Langendorf, J., Grosso, C., Lamb, J., Ivanov, S., Kustas, J., Jauregui, L., Preger, Y., & Torres-Castro, L. (2021). Overcharge tolerance of LiFePO4 cathode pouch cells. *Meeting Abstracts/Meeting Abstracts (Electrochemical Society. CD-ROM)*, *MA2021-02*(3), 246. https://doi.org/10.1149/ma2021-023246mtgabs

Beelen, H., Shivakumar, K. M., Raijmakers, L., Donkers, M., & Bergveld, H. J. (2020a). Towards impedance-based temperature estimation for Li-ion battery packs. *International Journal of Energy Research*, *44*(4), 2889–2908. https://doi.org/10.1002/er.5107

Beelen, H., Shivakumar, K. M., Raijmakers, L., Donkers, M., & Bergveld, H. J. (2020b). Towards impedance-based temperature estimation for Li-ion battery packs. *International Journal of Energy Research*, *44*(4), 2889–2908. https://doi.org/10.1002/er.5107

Cai, T., Stefanopoulou, A. G., & Siegel, J. B. (2019). Early Detection for Li-Ion Batteries Thermal runaway based on gas sensing. *ECS Transactions*, *89*(1), 85–97. https://doi.org/10.1149/08901.0085ecst

Cai, T., Valecha, P., Tran, V., Engle, B., Stefanopoulou, A., & Siegel, J. (2020). Detection of Li-ion battery failure and venting with carbon dioxide sensors. *eTransportation*, *7*, 100100. https://doi.org/10.1016/j.etran.2020.100100

Carkhuff, B. G., Demirev, P. A., & Srinivasan, R. (2018). Impedance-based battery management system for safety monitoring of lithium-ion batteries. *IEEE Transactions on Industrial Electronics*, *65*(8), 6497–6504. https://doi.org/10.1109/tie.2017.2786199

Case, S. (2022, November 13). *What we've learned after 2 years of Chevy Bolt recall: Over half of 2017 to 2021 Bolts have recorded a battery replacement*. [Web page]. InsideEVs. https://insideevs.com/news/621377/two-years-after-chevy-bolt-recall/

Challoob, A. F., Rahmat, N. a. B., Ramachandaramurthy, V. K. A., & Humaidi, A. J. (2023). Energy and battery management systems for electrical vehicles: A comprehensive review & recommendations. *Energy Exploration & Exploitation*, *42*(1), 341–372. https://doi.org/10.1177/01445987231211943

Christophersen, J. P., Morrison, J., Morrison, W., & Motloch, C. (2012). Rapid impedance spectrum measurements for state-of-health assessment of energy storage devices. *SAE International Journal of Passenger Cars. Electronic and Electrical Systems*, *5*(1), 246–256. https://doi.org/10.4271/2012-01-0657

Dong, P., Liu, Z., Wu, P., Li, Z., Wang, Z., & Zhang, J. (2021). Reliable and early warning of lithium-ion battery thermal runaway based on electrochemical impedance spectrum. *Journal of the Electrochemical Society*, *168*(9), 090529. https://doi.org/10.1149/1945-7111/ac239b

Doughty, D. H., Butler, P. C., Jungst, R. G., & Roth, E. (2002). Lithium battery thermal models. *Journal of Power Sources*, *110*(2), 357–363. https://doi.org/10.1016/s0378-7753(02)00198-2

Du Pasquier, A., Disma, F., Bowmer, T., Gozdz, A. S., Amatucci, G., & Tarascon, J. (1998). Differential scanning calorimetry study of the reactivity of carbon anodes in plastic li-ion batteries. *Journal of the Electrochemical Society*, *145*(2), 472–477. https://doi.org/10.1149/1.1838287

Duan, X., Wang, H., Jia, Y., Wang, L., Liu, B., & Xu, J. (2021). A multiphysics understanding of internal short circuit mechanisms in lithium-ion batteries upon mechanical stress abuse. *Energy Storage Materials*, *45*, 667–679. https://doi.org/10.1016/j.ensm.2021.12.018

Essl, C., Seifert, L., Rabe, M., & Fuchs, A. (2021). Early Detection of Failing Automotive Batteries Using Gas Sensors. *Batteries*, *7*(2), 25. https://doi.org/10.3390/batteries7020025

Feng, X., Ouyang, M., Liu, X., Lu, L., Xia, Y., & He, X. (2017). Thermal runaway mechanism of lithium ion battery for electric vehicles: A review. *Energy Storage Materials*, *10*, 246–267. https://doi.org/10.1016/j.ensm.2017.05.013

Feng, X., Sun, J., Ouyang, M., Wang, F., He, X., Lu, L., & Peng, H. (2014). Characterization of penetration induced thermal runaway propagation process within a large format lithium ion battery module. *Journal of Power Sources*, *275*, 261–273. https://doi.org/10.1016/j.jpowsour.2014.11.017

Fernandes, Y., Bry, A., & De Persis, S. (2018). Identification and quantification of gases emitted during abuse tests by overcharge of a commercial Li-ion battery. *Journal of Power Sources*, *389*, 106–119. https://doi.org/10.1016/j.jpowsour.2018.03.034

Gachot, G., Ribière, P., Mathiron, D., Grugeon, S., Armand, M., Leriche, J., Pilard, S., & Laruelle, S. (2010). Gas chromatography/mass spectrometry as a suitable tool for the li-ion battery electrolyte degradation mechanisms study. *Analytical Chemistry*, *83*(2), 478–485. https://doi.org/10.1021/ac101948u

Gao, T., Bai, J., Ouyang, D., Wang, Z., Bai, W., Mao, N., & Zhu, Y. (2022). Effect of aging temperature on thermal stability of lithium-ion batteries: Part A – High-temperature aging. *Renewable Energy*, *203*, 592–600. https://doi.org/10.1016/j.renene.2022.12.092

Giegerich, M., Akdere, M., Freund, C., Fuhner, T., Grosch, J., Koffel, S., Schwarz, R., Waldhor, S., Wenger, M., Lorentz, V., & Marz, M. (2016). Open, flexible and extensible battery management system for lithium-ion batteries in mobile and stationary applications. *Proceedings of the International Symposium on Industrial Electronics*. https://doi.org/10.1109/isie.2016.7745026

Golubkov, A. W., Fuchs, D., Wagner, J., Wiltsche, H., Stangl, C., Fauler, G., Voitic, G., Thaler, A., & Hacker, V. (2013). Thermal-runaway experiments on consumer Li-ion batteries with metal-oxide and olivin-type cathodes. *RSC Advances*, *4*(7), 3633–3642. https://doi.org/10.1039/c3ra45748f

Gutman, M., Sweeney, S., & Pereira. (2022, October 20). *Hurricane Ian flood damage to EVs creating ticking time bombs in Florida*. [Web page.]. ABC News Network. https://abcnews.go.com/US/hurricane-ian-flood-damage-evs-creating-ticking-time/story?id=91795016

Habib, A.., Hasan, M. K., Issa, G. F., Singh, D., Islam, S., & Ghazal, T. M. (2023). Lithium-ion battery management system for electric vehicles: constraints, challenges, and recommendations. *Batteries*, *9*(3), 152. https://doi.org/10.3390/batteries9030152

Haik, O., Ganin, S., Gershinsky, G., Zinigrad, E., Markovsky, B., Aurbach, D., & Halalay, I. (2011). On the thermal behavior of lithium intercalated graphites. *Journal of the Electrochemical Society*, *158*(8), A913. https://doi.org/10.1149/1.3598173

Hendricks, C., Williard, N., Mathew, S., & Pecht, M. (2015). A failure modes, mechanisms, and effects analysis (FMMEA) of lithium-ion batteries. *Journal of Power Sources*, *297*, 113–120. https://doi.org/10.1016/j.jpowsour.2015.07.100

Huang, Z., Yu, D., Makuza, B., Tian, Q., Guo, X., & Zhang, K. (2022). Hydrogen reduction of spent lithium-ion battery cathode material for metal recovery: Mechanism and kinetics. *Frontiers in Chemistry*, *10*. https://doi.org/10.3389/fchem.2022.1019493

Ishikawa, H., Mendoza, O., Sone, Y., & Umeda, M. (2011). Study of thermal deterioration of lithium-ion secondary cell using an accelerated rate calorimeter (ARC) and AC impedance method. *Journal of Power Sources*, *198*, 236–242. https://doi.org/10.1016/j.jpowsour.2011.09.067

Jhu, C., Wang, Y., Wen, C., Chiang, C., & Shu, C. (2011). Self-reactive rating of thermal runaway hazards on 18650 lithium-ion batteries. *Journal of Thermal Analysis and Calorimetry*, *106*(1), 159–163. https://doi.org/10.1007/s10973-011-1452-6

Jia, Z., Qin, P., Li, Z., Wei, Z., Jin, K., Jiang, L., & Wang, Q. (2022). Analysis of gas release during the process of thermal runaway of lithium-ion batteries with three different cathode materials. *Journal of Energy Storage*, *50*, 104302. https://doi.org/10.1016/j.est.2022.104302

Jiang, J., & Dahn, J. (2004). Effects of solvents and salts on the thermal stability of LiC6. *Electrochimica Acta*, *49*(26), 4599–4604. https://doi.org/10.1016/j.electacta.2004.05.014

Jin, Y., Zheng, Z., Wei, D., Jiang, X., Lu, H., Sun, L., Tao, F., Guo, D., Liu, Y., Gao, J., & Cui, Y. (2020). Detection of micro-scale li dendrite via h2 gas capture for early safety warning. *Joule*, *4*(8), 1714–1729. https://doi.org/10.1016/j.joule.2020.05.016

Lamb, J., & Orendorff, C. J. (2013). Evaluation of mechanical abuse techniques in lithium ion batteries. *Journal of Power Sources*, *247*, 189–196. https://doi.org/10.1016/j.jpowsour.2013.08.066

Lamb, J., Orendorff, C. J., Roth, E. P., & Langendorf, J. (2015). Studies on the thermal breakdown of common li-ion battery electrolyte components. *Journal of the Electrochemical Society*, *162*(10), A2131–A2135. https://doi.org/10.1149/2.0651510jes

Lamb, J., Torres-Castro, L., Hewson, J. C., Shurtz, R. C., & Preger, Y. (2021). Investigating the role of energy density in thermal runaway of lithium-ion batteries with accelerating rate calorimetry. *Journal of the Electrochemical Society*, *168*(6), 060516. https://doi.org/10.1149/1945-7111/ac0699

Lammer, M., Königseder, A., & Hacker, V. (2017). Holistic methodology for characterisation of the thermally induced failure of commercially available 18650 lithium ion cells. *RSC Advances*, *7*(39), 24425–24429. https://doi.org/10.1039/c7ra02635h

Larsson, F., & Mellander, B. (2014). Abuse by External Heating, Overcharge and short circuiting of commercial lithium-ion battery cells. *Journal of the Electrochemical Society*, *161*(10), A1611–A1617. https://doi.org/10.1149/2.0311410jes

Li, H., Zhou, D., Zhang, M., Liu, B., & Zhang, C. (2022). Multi-field interpretation of internal short circuit and thermal runaway behavior for lithium-ion batteries under mechanical abuse. *Energy*, *263*, 126027. https://doi.org/10.1016/j.energy.2022.126027

Liao, Z., Zhang, S., Li, K., Zhang, G., & Habetler, T. G. (2019). A survey of methods for monitoring and detecting thermal runaway of lithium-ion batteries. *Journal of Power Sources*, *436*, 226879. https://doi.org/10.1016/j.jpowsour.2019.226879

Liu, X., Yin, L., Ren, D., Wang, L., Ren, Y., Xu, W., Lapidus, S., Wang, H., He, X., Chen, Z., Xu, G., Ouyang, M., & Amine, K. (2021). In situ observation of thermal-driven degradation and safety concerns of lithiated graphite anode. *Nature Communications*, *12*(1). https://doi.org/10.1038/s41467-021-24404-1

Lyu, N., Jin, Y., Xiong, R., Miao, S., & Gao, J. (2021). Real-time overcharge warning and early thermal runaway prediction of li-ion battery by online impedance measurement. *IEEE Transactions on Industrial Electronics*, *69*(2), 1929–1936. https://doi.org/10.1109/tie.2021.3062267

Messing, M., Shoa, T., & Habibi, S. (2021). Electrochemical impedance spectroscopy with practical rest-times for battery management applications. *IEEE Access*, *9*, 66989–66998. https://doi.org/10.1109/access.2021.3077211

Metzger, M., Strehle, B., Solchenbach, S., & Gasteiger, H. A. (2016). Origin of H2Evolution in LIBs: H2O reduction vs. electrolyte oxidation. *Journal of the Electrochemical Society*, *163*(5), A798–A809. https://doi.org/10.1149/2.1151605jes

Mishra, S., Swain, S. C., & Samantaray, R. K. (2021). A review on battery management system and its application in electric vehicle. *2021 International Conference on Advances in Computing and Communications (ICACC)*. https://doi.org/10.1109/icacc-202152719.2021.9708114

Olabi, A., Maghrabie, H. M., Adhari, O. H. K., Sayed, E. T., Yousef, B. A., Salameh, T., Kamil, M., & Abdelkareem, M. A. (2022). Battery thermal management systems: Recent progress and challenges. *International Journal of Thermofluids*, *15*, 100171. https://doi.org/10.1016/j.ijft.2022.100171

Pastor-Fernández, C., Uddin, K., Chouchelamane, G. H., Widanage, W. D., & Marco, J. (2017). A comparison between electrochemical impedance spectroscopy and incremental capacity-differential voltage as Li-ion diagnostic techniques to identify and quantify the effects of degradation modes within battery management systems. *Journal of Power Sources*, *360*, 301–318. https://doi.org/10.1016/j.jpowsour.2017.03.042

Patil, M. S., Seo, J., & Lee, M. (2020). A novel dielectric fluid immersion cooling technology for Li-ion battery thermal management. *Energy Conversion and Management*, *229*, 113715. https://doi.org/10.1016/j.enconman.2020.113715

Qiu, M., Liu, J., Cong, B., & Cui, Y. (2023). Research progress in thermal runaway vent gas characteristics of Li-ion battery. *Batteries*, *9*(8), 411. https://doi.org/10.3390/batteries9080411

Raijmakers, L., Shivakumar, K., Donkers, M., Lammers, M., & Bergveld, H. (2016). Crosstalk interferences on impedance measurements in battery packs. *IFAC-PapersOnLine*, *49*(11), 42–47. https://doi.org/10.1016/j.ifacol.2016.08.007

Rask, E., Pavlich, C., Stutenberg, K., Duoba, M., & Keller, G. (2020, February). *Stranded energy assessment techniques and tools* (Report No. DOT HS 812 789). National Highway Traffic Safety Administration. https://rosap.ntl.bts.gov/view/dot/43941/-dot_43941_DS1.pdf

Ren, D., Feng, X., Lu, L., Ouyang, M., Zheng, S., Li, J., & He, X. (2017). An electrochemical-thermal coupled overcharge-to-thermal-runaway model for lithium ion battery. *Journal of Power Sources*, *364*, 328–340. https://doi.org/10.1016/j.jpowsour.2017.08.035

Sanitha, M. C., Chithra, M., Nithara, P. V., & Eldho, R. P. (2022, December 13-15). *Overview on battery management system and energy storage system of electric vehicle*. 2022 International Conference on Automation, Computing and Renewable Systems, Pudukkottai, India. https://doi.org/10.1109/icacrs55517.2022.10029266

Shen, H., Wang, H., Li, M., Li, C., Zhang, Y., Li, Y., Yang, X., Feng, X., & Ouyang, M. (2023). Thermal runaway characteristics and gas composition analysis of lithium-ion batteries with different LFP and NCM cathode materials under inert atmosphere. *Electronics*, *12*(7), 1603. https://doi.org/10.3390/electronics12071603

Spotnitz, R. M., Weaver, J., Yeduvaka, G., Doughty, D., & Roth, E. (2006). Simulation of abuse tolerance of lithium-ion battery packs. *Journal of Power Sources*, *163*(2), 1080–1086. https://doi.org/10.1016/j.jpowsour.2006.10.013

Srinivasan, R., Carkhuff, B. G., Butler, M. H., & Baisden, A. C. (2011). Instantaneous measurement of the internal temperature in lithium-ion rechargeable cells. *Electrochimica Acta*, *56*(17), 6198–6204. https://doi.org/10.1016/j.electacta.2011.03.136

Srinivasan, R., Demirev, P. A., & Carkhuff, B. G. (2018). Rapid monitoring of impedance phase shifts in lithium-ion batteries for hazard prevention. *Journal of Power Sources*, *405*, 30–36. https://doi.org/10.1016/j.jpowsour.2018.10.014

Sun, J., Li, J., Zhou, T., Yang, K., Wei, S., Tang, N., Dang, N., Li, H., Qiu, X., & Chen, L. (2016). Toxicity, a serious concern of thermal runaway from commercial Li-ion battery. *Nano Energy*, *27*, 313–319. https://doi.org/10.1016/j.nanoen.2016.06.031

Sun, Z., Guo, Y., Zhang, C., Xu, H., Zhou, Q., & Wang, C. (2022). A novel hybrid battery thermal management system for prevention of thermal runaway propagation. *IEEE Transactions on Transportation Electrification*, *9*(4), 5028–5038. https://doi.org/10.1109/tte.2022.3215691

Tang, X., Zhang, G., Wang, X., Wei, G., Han, G., Zhu, J., Wei, X., & Dai, H. (2021). Investigating the critical characteristics of thermal runaway process for LiFePO4/graphite batteries by a ceased segmented method. *iScience*, *24*(10), 103088. https://doi.org/10.1016/j.isci.2021.103088

Waag, W., Fleischer, C., & Sauer, D. U. (2014). Critical review of the methods for monitoring of lithium-ion batteries in electric and hybrid vehicles. *Journal of Power Sources*, *258*, 321–339. https://doi.org/10.1016/j.jpowsour.2014.02.064

Wang, L., Zhao, X., Deng, Z., & Yang, L. (2022). Application of electrochemical impedance spectroscopy in battery management system: State of charge estimation for aging batteries. *Journal of Energy Storage*, *57*, 106275. https://doi.org/10.1016/j.est.2022.106275

Wang, Q., Mao, B., Stoliarov, S. I., & Sun, J. (2019). A review of lithium ion battery failure mechanisms and fire prevention strategies. *Progress in Energy and Combustion Science*, *73*, 95–131. https://doi.org/10.1016/j.pecs.2019.03.002

Wang, Q., Ping, P., Zhao, X., Chu, G., Sun, J., & Chen, C. (2012). Thermal runaway caused fire and explosion of lithium ion battery. *Journal of Power Sources*, *208*, 210–224. https://doi.org/10.1016/j.jpowsour.2012.02.038

Wang, Y., Gao, Q., Wang, G., Lu, P., Zhao, M., & Bao, W. (2018). A review on research status and key technologies of battery thermal management and its enhanced safety. *International Journal of Energy Research*, *42*(13), 4008–4033. https://doi.org/10.1002/er.4158

Wei, J., Dong, G., & Chen, Z. (2019). Model-based fault diagnosis of Lithium-ion battery using strong tracking extended Kalman filter. *Energy Procedia*, *158*, 2500–2505. https://doi.org/10.1016/j.egypro.2019.01.391

Xia, B., & Mi, C. (2016). A fault-tolerant voltage measurement method for series connected battery packs. *Journal of Power Sources*, *308*, 83–96. https://doi.org/10.1016/j.jpowsour.2016.01.057

Xia, Q., Ren, Y., Wang, Z., Yang, D., Yan, P., Wu, Z., Sun, B., Feng, Q., & Qian, C. (2022). Safety risk assessment method for thermal abuse of lithium-ion battery pack based on multiphysics simulation and improved bisection method. *Energy*, *264*, 126228. https://doi.org/10.1016/j.energy.2022.126228

Xu, F., He, H., Liu, Y., Dun, C., Ren, Y., Liu, Q., Wang, M., & Xie, J. (2012). Failure Investigation of LiFePO4 cells under overcharge conditions. *Journal of the Electrochemical Society*, *159*(5), A678–A687. https://doi.org/10.1149/2.024206jes

Yang, H., Bang, H., Amine, K., & Prakash, J. (2004). Investigations of the exothermic reactions of natural graphite anode for li-ion batteries during thermal runaway. *Journal of the Electrochemical Society*, *152*(1), A73. https://doi.org/10.1149/1.1836126

Yuan, C., Wang, Q., Wang, Y., & Zhao, Y. (2019). Inhibition effect of different interstitial materials on thermal runaway propagation in the cylindrical lithium-ion battery module. *Applied Thermal Engineering*, *153*. https://doi.org/10.1016/j.applthermaleng.2019.02.127

Yuan, L., Dubaniewicz, T., Zlochower, I., Thomas, R., & Rayyan, N. (2020). Experimental study on thermal runaway and vented gases of lithium-ion cells. *Process Safety and Environmental Protection*, *144*, 186–192. https://doi.org/10.1016/j.psep.2020.07.028

Zhang, B., Bewley, R. L., Tanim, T. R., & Walker, L. K. (2022). Electric vehicle post-crash Recovery—Stranded energy issues and mitigation strategy. *Journal of Power Sources*, *552*, 232239. https://doi.org/10.1016/j.jpowsour.2022.232239

Zhang, Q., Niu, J., Zhao, Z., & Wang, Q. (2021). Research on the effect of thermal runaway gas components and explosion limits of lithium-ion batteries under different charge states. *Journal of Energy Storage*, *45*, 103759. https://doi.org/10.1016/j.est.2021.103759

Zhang, S. S. (2014). Insight into the gassing problem of li-ion battery. *Frontiers in Energy Research*, *2*. https://doi.org/10.3389/fenrg.2014.00059

This page is intentionally left blank.

Appendix A: Battery Advanced Diagnostics Evaluation (Badge) Platform

Battery Advanced Diagnostics Evaluation (Badge) Platform

BADGE Concept

The platform is an open architecture platform that can operate in real-time and be reconfigurable to support new and potentially novel Management and Diagnostic (M&D) technologies. The development of BADGE was carried out at INL and supported through technical and experimental feedback from SNL. The platform has the flexibility to accommodate commercial-off-the-shelf diagnostics, and near commercial technologies which use different communication protocols. The platform allows for the evaluation of single cells, packs, modules, or like systems through integrated diagnostic tools (i.e., specific electrical circuits that simulate key failure pathways), in normal and off-normal conditions to verify the diagnostic's detectable range and fidelity. Off-normal states specific to a device may include capacity and impedance imbalance, internal and external shorts, mild OC/overdischarge, over-temperature, non-uniform temperature, thermal runaway, failure propagation, etc., in single cell and/or multi-cell configurations. The platform can accommodate different battery chemistry and configurations with independent monitoring of the cell, module, pack levels, and/or diagnostic systems. Detecting response from a single cell or a small subset of cells is a key feature of the platform to narrow down a problematic cell or string within a pack. The platform provides provisions to examine the resilience of the diagnostic system under realistic in-vehicle operating conditions (e.g., high-rate charging or discharging, temperature extremes, vibration) in short-term or long-term test settings. Figure 34, presents the conceptual layout of the BADGE platform.

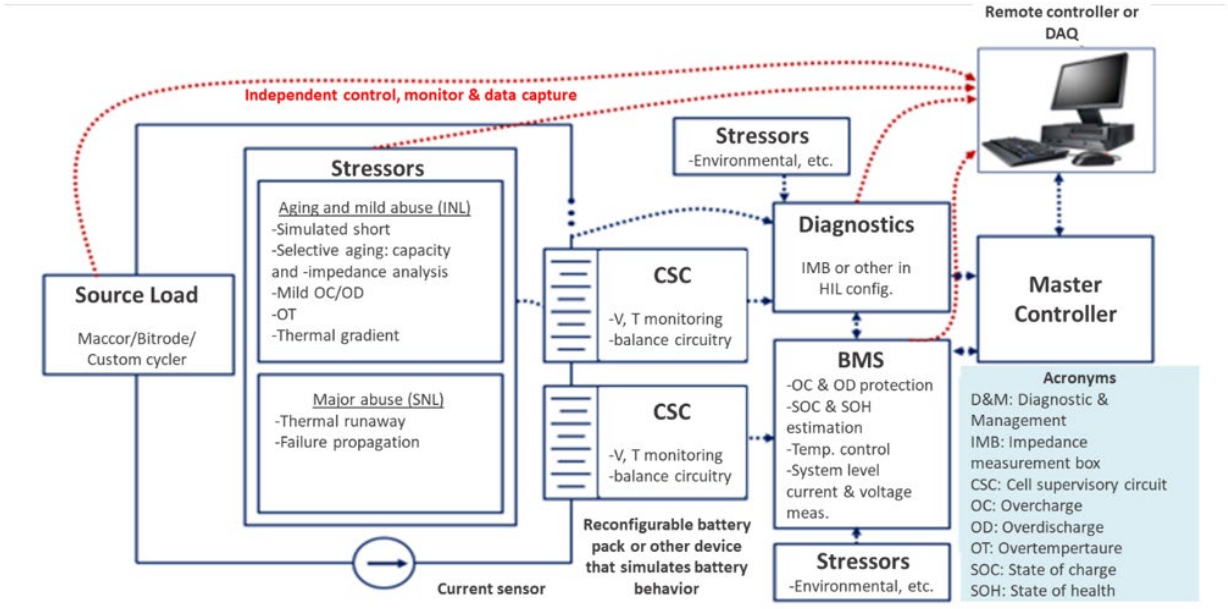

Figure 34. Conceptual layout of the BADGE platform.

BADGE Platform Development

The procured hardware was selected to support all aspects of the platform. With that in mind, a multicore controller acts as the main controller, battery-emulator controller, and remote data DAQ controller. The controller is a Peripheral Component Interconnect eXtensions for Instrumentation (PXI) controller from National Instruments and allows for flexibility. All DAQ and communications hardware is also PXI-based for seamless integration with the PXI controller. The communication systems that have been added to the PXI unit are RS232, RS485, USB, Ethernet, and General-Purpose Interface Bus for instrument control and CAN and Local Interconnect Network for vehicle and BMS control. A reconfigurable DAQ system has been added that has analog input, output, and TC connections. Figure 35 shows how different communications were implemented using the PXI unit.

Most vehicles use either CAN or LIN as an onboard communication protocol. As a result, communication within a battery system uses one of these protocols. Because it is unknown what communication protocol a future diagnostic will use, the protocols chosen will allow for onboard and standalone diagnostic systems. Figure 3 shows a selection of hardware purchased for use with the PXI unit. The platform will include six main software components, as shown in Figure 36 (top)—namely, the DAQ engine, data analysis/collection, BMS hardware interface, user/operator interface, and diagnostic hardware interface.

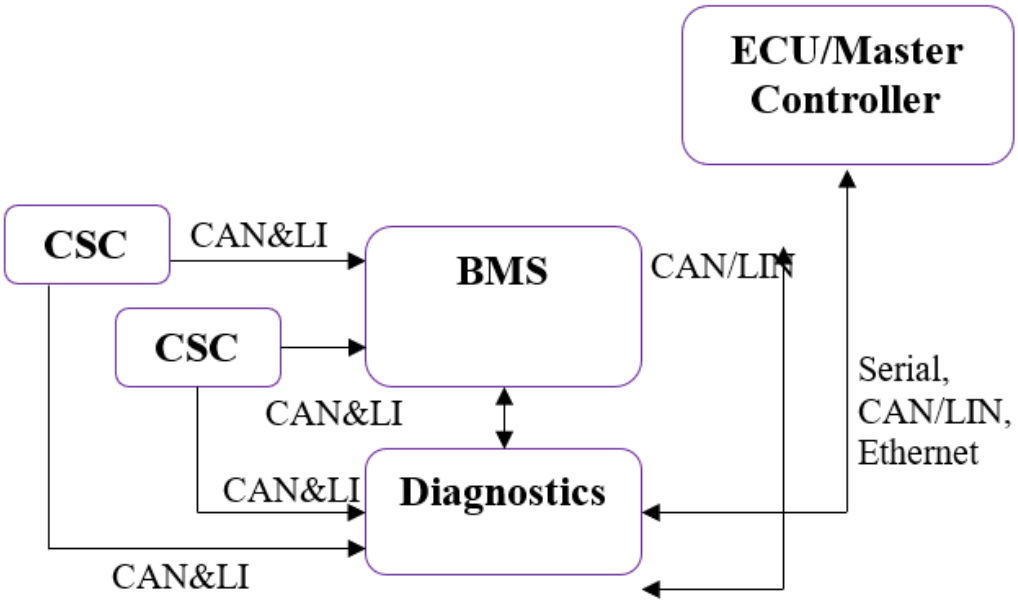

Figure 35. BMS functionality and communication capability

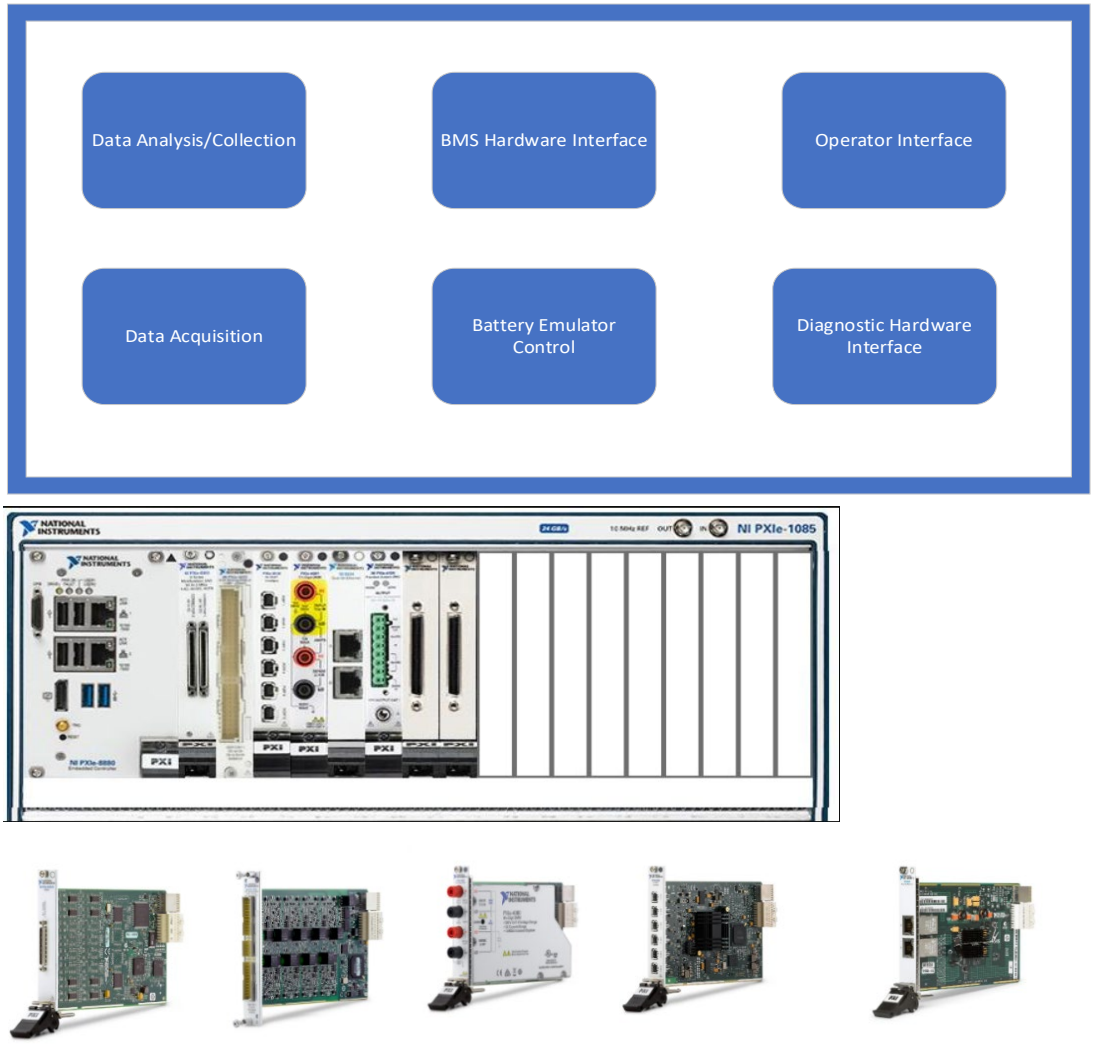

Figure 36. Hardware components procured for the BADGE platform

The Gen1 version of the BADGE platform is shown in Figure 37. The graphical user interphase of the platform is shown in the top image of Figure 38 and the data output screen in the bottom image of Figure 38, displaying multiple synchronized signals. In this version of the BADGE platform, the PXI controller seamlessly communicates with the Maccor battery tester and other diagnostics devices such as a Solartron EIS, iRIS rapid EIS, various gas-based diagnostics, and high precision source measure unit (SMU). The platform communicates with the Maccor cycler via a CAN network. Triggers can be set to enable selective high-rate data capture based on input from the Maccor or other diagnostic systems. The platform is equipped with high resolution analog inputs that can be used to measure temperature, pressure, voltage, current, etc., as well as digital input/output channels that can be used to trigger external devices. The Dynexus iRIS system, which takes rapid EIS measurements, can be automatically triggered by the platform.

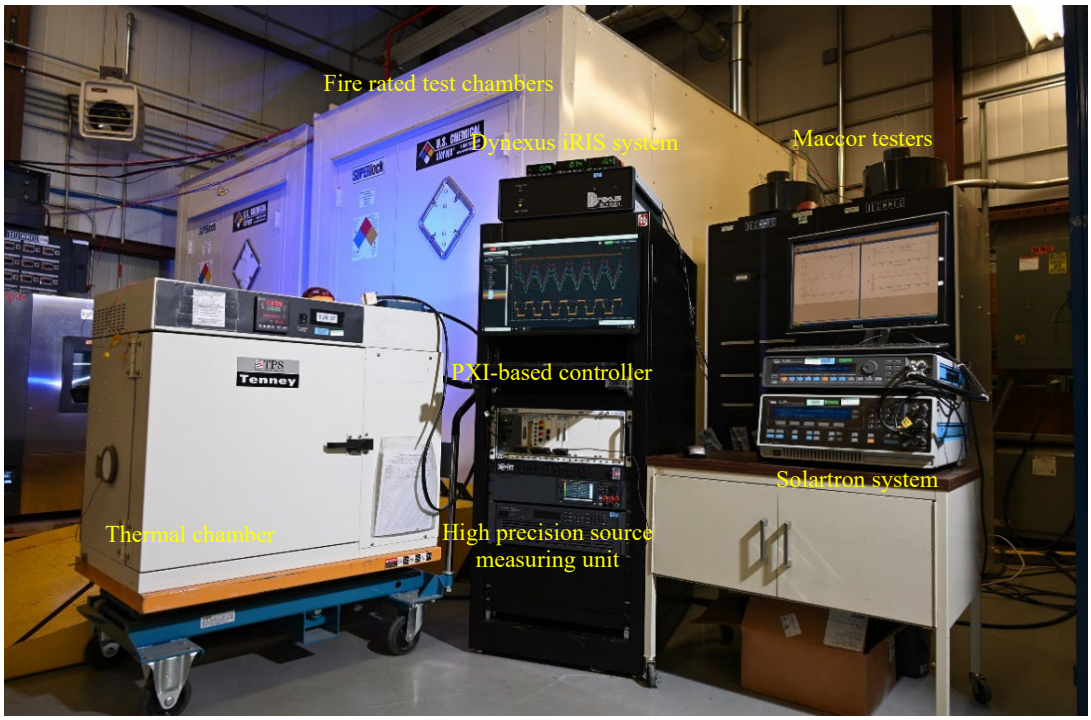

Figure 37. BADGE platform developed at INL for comprehensive battery pack diagnostics

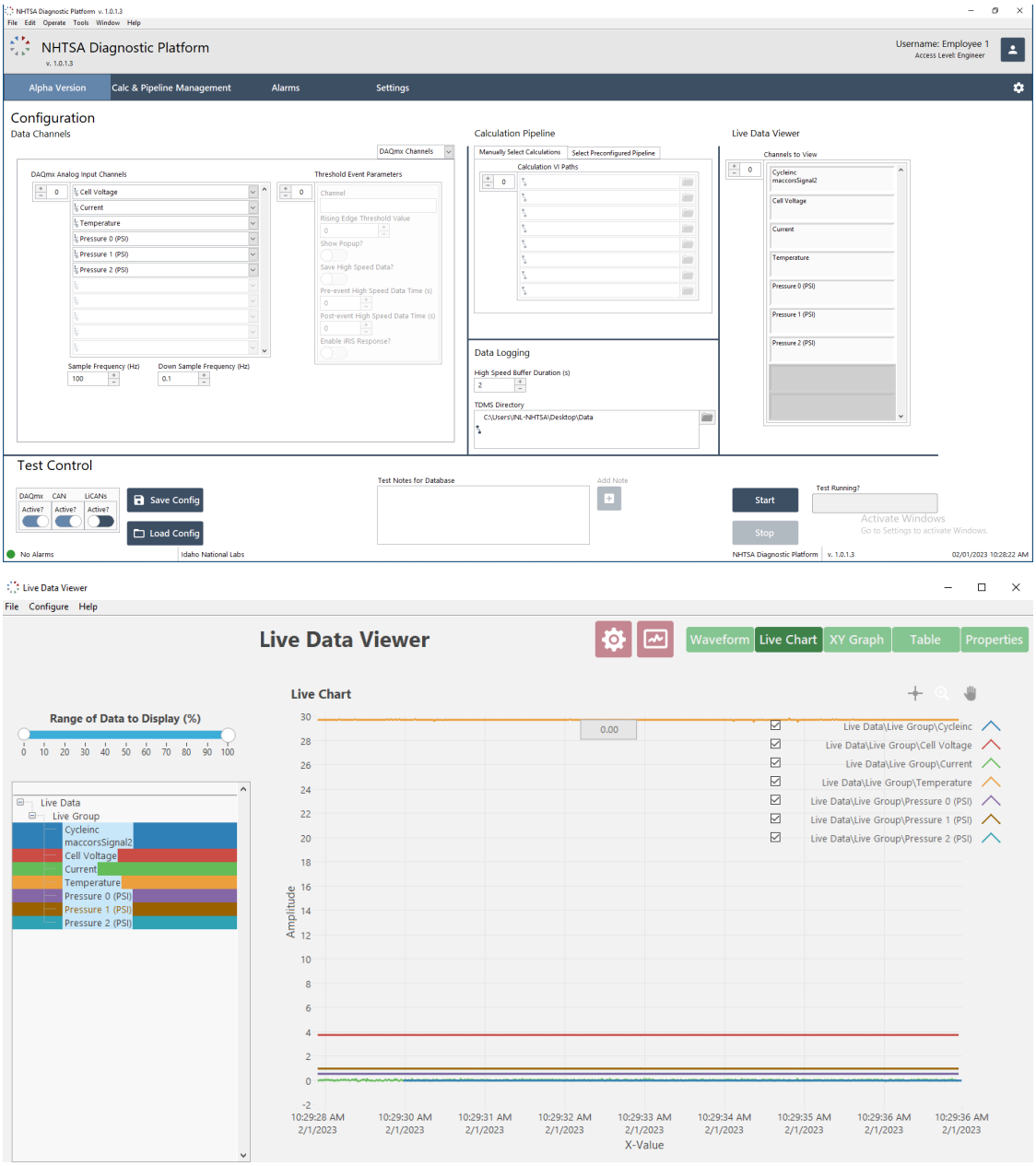

Figure 38. Graphical user interphase of the BADGE platform

The platform includes a high precision SMU. A LabVIEW program has been developed to communicate with and control the SMU. The LabVIEW block diagram is shown in Figure 39. This enables the platform to accurately measure very low leakage currents and quantify battery self-discharge, allowing for the benchmarking of existing/emerging leakage current detection diagnostics. Using this LabVIEW program, the SMU can also function as a high precision battery cycler. The implemented M&D devices and methods that are, to-date, compatible with BADGE include: EIS measurement from Solartron Analytical, iRIS EIS from Dynexus Technology, gas sensors using serial/CAN/analog/digital communication protocols, a high precision SMU, and standard data collection tools (e.g., voltage, current, temperature, and

pressure). Additional diagnostics on the roadmap for inclusion are Cadex Spectro EIS and Novus Sentry short detection.

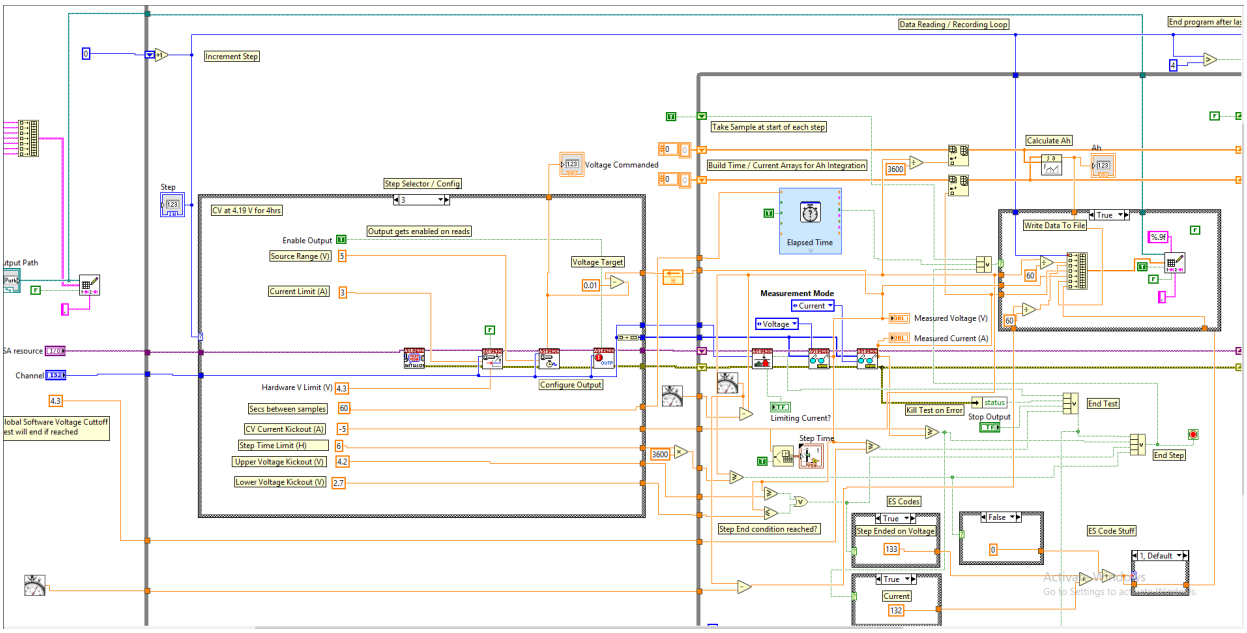

Figure 39. LabVIEW block diagram used to control the SMU

This page is intentionally left blank.

DOT HS 813 671
January 2026

U.S. Department
of Transportation

**National Highway
Traffic Safety
Administration**

16527-011326-v4a